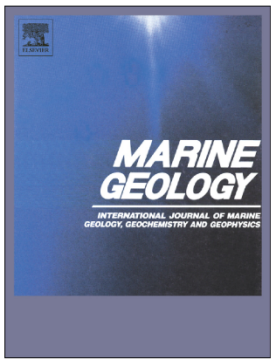

Deep Sulfate-Methane-Transition and sediment diagenesis in the Gulf of Alaska (IODP Site U1417)

Mark Zindorf, Christian März, Thomas Wagner, Sean P.S. Gulick, Harald Strauss, Jeff Benowitz, John Jaeger, Bernhard Schnetger, Laurel Childress, Leah LeVay, Cees van der Land, Michelle La Rosa

PII: S0025-3227(19)30143-4
DOI: https://doi.org/10.1016/j.margeo.2019.105986
Article Number: 105986
Reference: MARGO 105986

To appear in: *Marine Geology*

Received date: 23 March 2019
Revised date: 3 July 2019
Accepted date: 8 July 2019

Please cite this article as: M. Zindorf, C. März, T. Wagner, et al., Deep Sulfate-Methane-Transition and sediment diagenesis in the Gulf of Alaska (IODP Site U1417), Marine Geology, https://doi.org/10.1016/j.margeo.2019.105986

Deep Sulfate-Methane-Transition and sediment diagenesis in the Gulf of Alaska (IODP Site U1417)

Authors

Mark Zindorf[1]*, Christian März[1,2], Thomas Wagner[1,3], Sean P.S. Gulick[4], Harald Strauss[5], Jeff Benowitz[6], John Jaeger[7], Bernhard Schnetger[8], Laurel Childress[9], Leah LeVay[9], Cees van der Land[1], Michelle La Rosa[8]

Corresponding author: Mark Zindorf, e-mail: mzindorf@ifremer.fr

Affiliations

[1]School of Natural and Environmental Sciences, Newcastle University, NE1 7RU Newcastle upon Tyne, United Kingdom
*Current address: Ifremer - Centre de Brest, Laboratoire Environnement Profond, Technopôle Brest-Iroise BP 70, 29280 Plouzané, France

[2]School of Earth and Environment, University of Leeds, LS2 9JT Leeds, United Kingdom

[3]The Lyell Centre, School of Energy Geoscience Infrastructure and Society, Heriot-Watt University, EH14 4HS Edinburgh, United Kingdom

[4]Institute for Geophysics and Department of Geological Sciences, Jackson School of Geosciences, University of Texas at Austin, Austin, TX 78758-4445, USA

[5]Institut für Geologie und Paläontologie, Westfälische Wilhelms-Universität Münster, 48149 Münster, Germany

[6]Geophysical Institute, University of Alaska Fairbanks, Fairbanks, AK 99775, USA

[7]Department of Geological Sciences, University of Florida, Gainesville, FL 32611-2120, USA

[8]Institut für Chemie und Biologie des Meeres (ICBM), Universität Oldenburg, 26129 Oldenburg, Germany

[9]International Ocean Discovery Program, Texas A&M University, College Station, TX 77845-9547, USA

Abstract

Sediment samples from the Gulf of Alaska (GOA, IODP Expedition 341, Site U1417) have been analyzed to understand present and past diagenetic processes that overprint the primary sediment composition. No Sulfate-Methane Transition Zone (SMTZ) was observed at the zone of sulfate depletion, but a > 200 m thick sulfate- and methane-free sediment interval occurred between the depth of sulfate depletion (~200 m) and the onset of methanogenesis (~440 m). We suggest that this apparent gap in biogeochemical processing of organic matter is caused by anaerobic oxidation of methane fueled by sulfate which is released during dissolution of barites at the upper boundary of the methane rich layer. Beneath the methanogenic zone, at ~650 m depth, pore-water sulfate concentrations increase again, indicating sulfate supply from greater depth feeding into a deep, inverse SMTZ. A likely explanation for the availability of sulfate in the deep sub-seafloor at U1417 is the existence of a deep aquifer related to plate bending fractures, which actively transports sulfate-rich water to, and potentially along, the interface between sediments and oceanic crust. Such inverse diagenetic zonations have been previously observed in marine sediments, but have not yet been linked to subduction-related plate bending. With the discovery of a deep inverse SMTZ in an intra-oceanic plate setting and the blocking of upward methane diffusion by sulfate released from authigenic barite dissolution, Site U1417 provides new insights into sub-seafloor pore-fluid and gas dynamics, and their implications for global element cycling and the deep biosphere.

Keywords

Early diagenesis, Sulfate-Methane Transition Zone, Sulfur isotopes, Inverse diagenetic zonation, Gulf of Alaska, IODP

1. Introduction

Early diagenesis plays an important role in global carbon (C) cycling by controlling the amount of organic C preserved in the sediment or recycled by microbial activity. Remineralization of organic matter (OM) follows a succession of microbially mediated redox reactions with organic carbon as the electron donor, and the electron acceptors oxygen, nitrate, manganese (oxyhydr)oxides, iron (oxyhydr)oxides and sulfate. Once all electron acceptors are depleted, the remaining OM is converted to methane (Froelich et al., 1979; Jørgensen, 2006). This so-called catabolic sequence follows the decreasing energy yields of the microbially mediated redox reactions (Froelich et al., 1979), with energetically less favorable sulfate reduction and methanogenesis occurring in the deeper parts of any sedimentary succession. The upper limit of the methanogenic zone is usually equivalent to the maximum depth of sulfate penetration into the sediments: In the Sulfate-Methane Transition Zone (SMTZ), an anaerobic, highly specialized bacteria-archaea consortium uses sulfate as an electron acceptor to anaerobically oxidize methane (Martens and Berner, 1977; Reeburgh, 1980; Niewöhner et al., 1998; Boetius et al., 2000). Despite the low energy yields provided by sulfate reduction and methanogenesis, these reactions account for most of the non-oxic OM decomposition in the global seafloor due to the high abundance of sulfate in seawater and pore-waters compared to other electron acceptors (Bowles et al., 2014). Thus, SMTZs exhibit significantly higher microbial

activity than surrounding sediments, and are biological and geochemical hotspots within the deep marine biosphere (Parkes et al., 2005; Harrison et al., 2009). SMTZs are also important biogeochemical reaction zones where distinct diagenetic signatures are generated.

At an SMTZ, sulfate reduction leads to the production of hydrogen sulfide which, in turn, causes the reduction of mostly terrigenous iron (oxyhydr)oxides and the formation of iron sulfides (most commonly pyrite, FeS_2). Beneath the SMTZ, barite ($BaSO_4$) dissolves in the sulfate-free pore-waters, but the released Ba^{2+} re-precipitates as authigenic barite from pore-water following its diffusion into or above the SMTZ (Von Breymann et al., 1992; Dickens, 2001; Kasten et al., 2001, 2012). Pyrite and barite are therefore common authigenic minerals at SMTZs, and their presence and isotopic compositions can be used to identify paleo-SMTZs in the geological record (Torres et al., 1996; Riedinger et al., 2006; Peketi et al., 2012).

Two major aspects of diagenetic processes in marine sediments are of continuing interest: non-steady state diagenesis (Kasten et al., 2003), and deviations from the classic catabolic sequence (Froelich et al., 1979). Non-steady state diagenesis occurs in settings where external forcing (including sedimentation rates, OM deposition, methane flux) is highly variable on timescales from days to millennia (Kasten et al., 2003). In such situations, spatial fixation of specific biogeochemical zones over centuries to millennia can lead to the persistence of certain diagenetic processes in defined sediment intervals (e.g. accumulation of authigenic minerals at the expense of primary minerals). These diagenetic processes need to be active (and hence external conditions need to be stable) for tens to thousands of years to generate measurable changes in sediment composition. On these timescales, changes to external forcing can be induced by a multitude of climatic or

oceanographic events. In deep-sea fan sediments, for example, changes can result from drastic episodic decreases in sedimentation rates on glacial-interglacial timescales (e.g. Kasten et al., 1998; Riedinger et al., 2005; März et al., 2008, 2018). In fact, in marine settings affected by cyclic variations in climatic forcing, non-steady state conditions appear to be the rule rather than the exception and often leave distinguishable geochemical imprints in the sediment record (Kasten et al., 2003 and references therein; Riedinger et al., 2005; Contreras et al., 2013).

Over the last years, it also emerged that the vertical catabolic redox succession, as proposed by Froelich et al. (1979), may not always apply in marine sediments. Prominent examples are inverse SMTZs where sulfate is supplied not from the overlying seawater, but from a sulfate pool located deeper in the sediment (DeLong, 2004). Inverse STMZs above the interface between sediments and the oceanic crust/basement have been reported from various sites, but have so far not been conclusively explained. Most of these sites are located in geodynamically active settings of the ocean, including mid-ocean ridge flanks, seamounts (e.g. ODP Site 1026 + IODP Site U1301, Engelen et al., 2008; ODP Sites 1225 and 1226, D'Hondt et al., 2003) or accretionary prisms (e.g. IODP Site C0012, Torres et al., 2015). Here, active hydrologic circulation provides sulfate-rich water to deeper sediment layers. Similar to conventional SMTZs, these inverse biogeochemical transitions are hotspots of deep microbial activity (e.g. DeLong, 2004; D'Hondt et al., 2004; Engelen et al., 2008).

One depositional setting where both non-steady state diagenesis and a deep source of sulfate can be observed is Site U1417 drilled during Expedition 341 of the Integrated Ocean Drilling Program (IODP) in the Gulf of Alaska (GOA, Figure 1). As reported by Jaeger et al. (2014) and Gulick et al. (2015), the site has experienced

several order-of-magnitude variations in sedimentation rate since the late Miocene, and the sediments appear to be significantly overprinted by diagenesis. Most remarkably, non-steady state diagenesis at this location is induced by methane consumption without contact to sulfate in the upper parts of the sediment succession. In addition, there is a significant and unusual occurrence of pore-water sulfate below the methanogenic zone, disconnected from the overlying seawater. Jaeger et al. (2014) postulated the existence of a deep inverse SMTZ at Site U1417, but both the source of the deep sulfate and its potential impact on diagenetic pathways are unconstrained. Detailed downhole geochemical analyses at Site U1417, coupled with regional geophysical imaging of the sub-seafloor, offer the possibility to explore these two aspects of diagenesis in a deep-sea setting.

Here, we present bulk sediment, pore-water and gas geochemical data from IODP Site U1417. We combine these data with sequential leaching of Fe and S species. Further, we use O- and H-indices as proxies of organic matter reactivity, and $\delta^{34}S$ data from pyrite to reveal the nature of the deep sulfate pool.

Furthermore, we compare our observations at Site U1417 to previously drilled ODP and IODP sites worldwide where similar observations have been made and to results from DSDP Site 178 drilled ~40 years earlier at nearly the same location as Site U1417 (Kulm and Von Huene, 1973).

2. Materials and Methods

In 2013, IODP Expedition 341 drilled Site U1417 to ~700 m sediment depth (recovery 70.1%) in the GOA at 56.96° N and 147.11° E (Figure 1, Jaeger et al., 2014). The site is located in 4200 m water depth on the Surveyor Fan. It is situated

approximately 60 km from the Surveyor Channel, which is the main sediment provider, ~70 km from the Kodiak-Bowie Seamount Chain to the southeast, and ~75 km from the Aleutian Trench to the northwest.

Holes A to E were cored at Site U1417 resulting in a continuous composite record of ~700 m length (core composite depth below sea floor, scale B; CCSF-B). Information from earlier Deep Sea Drilling Project (DSDP) Leg 18 Site 178 (Kulm and Von Huene, 1973), of which Site U1417 is a re-drill, and seismic reflection data (Reece et al., 2011) revealed that the sediment-basement boundary lies at 794 ± 74 m depth, and coring at Site U1417 was terminated ~50-100 m above basement (Figure 2). The age model for Site U1417 (Gulick et al., 2015) is based on paleomagnetics (14 datums), biostratigraphy (18 datums), and extrapolated to the basement. For this study, three basalt basal core samples from DSDP Site 178 were dated using the whole rock $^{40}Ar/^{39}Ar$ methods outlined in Benowitz et al. (2014), to attain a more robust age of the onset of sediment deposition at Site U1417. See supplementary text, figures and tables for more details on the $^{40}Ar/^{39}Ar$ methods and results. All dating points were included to construct minimum and maximum age models.

Immediately after sectioning the core, samples for pore-gas analyses were taken, sealed, and heated to 70°C. Headspace gas was captured and analyzed on board for methane, ethane, ethene, propane and propene using a Hewlett Packard 6890 gas chromatograph equipped with a 2.4 m × 3.2 mm stainless steel column packed with 100/120 mesh HayeSep R and a flame ionization detector. For methane, the coefficient of variation was 1 to 5% (Jaeger et al., 2014).

Pore-water from 72 whole-round core samples of 5 to 15 cm thickness was taken with variable depth resolution. The samples were squeezed at 5,000 to 30,000 psi (~

345 to 2070 bars) and the expressed water was filtered through 0.45 µm Whatman polyethersulfone disposable filters. On-board geochemical analyses were conducted with the following instrumentation: Alkalinity was determined by titration with 0.1 N HCl and 0.1 N $AgNO_3$ solutions, sulfate Ca^{2+} and Mg^{2+} concentrations were determined with a Metrohm 850 Professional ion chromatograph. Ammonium was determined with an Agilent Cary 100 double-beam UV/Vis spectrophotometer. Minor elements (Ba^{2+}, Fe^{2+}, Li^{+}, Sr^{2+}) were analyzed with a TeledyneProdigy high-dispersion inductively coupled plasma atomic emission spectroscopy (ICP-AES). Coefficient of variation for all cations and anions was 3 to 5% (Jaeger et al., 2014). Pore-water data are presented in micromolar (µM) or millimolar (mM), pore-gas in milimolar (mM) concentrations.

Onboard, total inorganic carbon (TIC) was measured with a UIC 5015 CO_2 coulometer. For this, 10 mg of freeze-dried sediment were reacted with 1M HCl and the liberated CO_2 was back-titrated to a colorimetric end point. TIC was converted into $CaCO_3$ by multiplying wt% TIC by 8.33 under the assumption that all TIC is present as $CaCO_3$. The coefficient of variation for this analysis was ~1%. (Jaeger et al., 2014).

For shore-based geochemical analyses, 163 sediment samples were taken at ~3 m resolution. This sampling strategy included splits of the pore-water squeeze cakes and additional discrete samples collected from working halves of the split cores. Sediment samples were either freeze-dried on board, or initially stored in vacuum sealed, gas-tight plastic bags with oxygen strippers followed by freeze-drying on shore.

On shore, splits of all sediment samples were homogenized using an agate mortar and pestle, and analyzed for Si, Al, Fe and Ba using a wavelength-dispersive XRF (Panalytical Axios max, 4 kW). For this, 700 mg of sample were mixed with 4200 mg di-lithiumtetraborate, pre-oxidized with 1g ammonium nitrate at 500° C and then fused to homogenous glass beads. Calibration of the XRF was done by using 52 SRM and in-house samples resulting in an average absolute error based on all 52 samples of 0.3 wt% Si (0.1), 0.1 wt% Al (0.2), 0.1 wt% Fe (0.2) and 31 mg/kg Ba (2) (in brackets: precision in % standard deviation for a typical sample). Total carbon (TC), total organic carbon (TOC) and total sulfur (TS) were quantified using Leco and Elementar combustion analyzers with a reproducibility better than 5% (TC) and 10% (TOC, TS), based on duplicates of every tenth sample. XRF, C and S data are presented as weight percent (wt%) or mg/kg of dry sediment. To account for depositional changes of the sedimentary matrix and dilution effects, chemical data are also reported as element to Al ratios.

A sequential Fe and S extraction scheme following the methods of Canfield et al. (1986), Poulton and Canfield (2005), and März et al. (2012) was applied to operationally separate iron carbonates, amorphous/poorly crystalline iron (oxyhydr)oxides, crystalline iron oxides, and magnetite as well as iron mono-sulfides (e.g. mackinawite, greigite) and pyrite. Iron carbonates were extracted with 1M Na-acetate at pH 4.5 for 24h, amorphous/poorly crystalline iron (oxyhydr)oxides with 1M hydroxylamine HCl and 25% acetic acid for 24h, crystalline iron oxides were extracted with a dithionite solution at pH 4.8 for 2h and magnetite was extracted with a 1M ammonium oxalate solution for 6h. Ten ml of each solution were applied to the same 0.1 g sample in sequence. For the S extraction, ~0.5 g of sample material were first boiled with 50 ml half-concentrated HCl for 45 min to dissolve all iron

mono-sulfides, then 12 ml fully reduced Cr(II)-chloride were added and boiled for another 45 min to oxidize pyrite. The resulting H_2S of both fractions was trapped as silver sulfide (Ag_2S), weighed and stochiometrically converted into amounts of Fe bound as FeS and FeS_2, respectively. The iron fractions resulting from the different extraction steps are presented as ratios of highly reactive Fe (FeHR, sum of Fe in all extraction steps) over total Fe (determined by XRF) (FeHR/FeT), and of sulfide-bound Fe (Fe-S, sum of Fe in mono-sulfides and pyrite) over highly reactive Fe (Fe-S/FeHR). The latter ratio indicates how much of the available FeHR has been converted into iron sulfides (Poulton et al., 2004). The reproducibility of the Fe extraction was within 5% for all four fractions, as determined from triplicate analyses of five samples. The standard error of the S extraction was within 20%, as determined by triplicate analysis of three randomly selected samples, mainly due to low total S contents (0.13 – 0.2 wt%) in these samples.

Following the S extraction, the isotopic composition of pyrite-bound S was determined on the precipitated silver sulfide. The two naturally most abundant S isotopes, ^{32}S and ^{34}S, were measured on 200 µg of silver sulfide homogenously mixed with 300-600 µg vanadium pentoxide using a ThermoFinnigan Delta Plus mass spectrometer coupled to a Carlo Erba Elemental Analyzer (EA-IRMS), as described in Strauss et al. (2012). Sulfur isotope compositions are presented in the standard delta notation ($\delta^{34}S$) as per mil difference to the international reference material Vienna Canyon Diablo Troilite (V-CDT). Standard deviation on duplicate measurements was, on average 0.3 ‰ and above 1 ‰ in one sample only. Analytical performance was monitored with international (IAEA S1, S2, S3, NBS 127) and in-house laboratory (Ag_2S) standards.

Another dataset of 7 samples below 600 m core depth (CCSF-B) was used to assess organic matter reactivity (Childress, 2016). These samples were taken independently from the above described sampling strategy and analyses. Subsamples for O- and H-index measurements were collected at ~15 m resolution and samples were stored frozen. Sediment samples were freeze-dried, after which a subsample of each was decarbonated via acidification with 4N HCl for 48 - 72 hours (Leithold and Blair, 2001). Subsamples of dried and ground marine sediments were analyzed by GeoMark Research using Rock-Eval 6 pyrolysis to determine the type and maturity of organic matter. The method consists of a programmed temperature heating to sequentially release free hydrocarbons, hydrocarbons generated by thermal cracking of nonvolatile organic matter, and CO_2 from kerogen. The resulting data are used to calculate H/C (hydrogen index) and O/C (oxygen index) ratios.

All pore-water and solid phase constituents are displayed against composite coring depth in meters below the sea floor on the CCSF-B scale (core composite depth below seafloor, a depth scale that is corrected for sediment expansion; Jaeger et al., 2014). In the following, all depth information refers to sediment depth unless stated otherwise.

3. Results

Sediment ages extend back to 16.5 Ma (early Miocene) at the deepest drilled point of Site U1417 (Jaeger et al., 2014). The new $^{40}Ar/^{39}Ar$ dating of the basal basalt lava flow samples from DSDP Site 178 provides an age of 25.80 ± 0.36 Ma. This disagrees with previous assumptions. Originally, the basement age at Site U1417 was assumed to be 37 – 41.2 Ma which is the estimated age of the mid oceanic

ridge basalt at this site (Jaeger et al., 2014). The new age determinations suggest that the basement at Site U1417 is formed by a younger overlying volcanic sill. The sediment at Site U1417 consists mainly of hemi-pelagic mud, distal turbidites, and interbedded layers of biosiliceous ooze (Jaeger et al., 2014).

The sulfate content of the pore-water decreases gradually from 27.5 mM at the top of the sediment column to values between 0 and 2 mM at ~200 m depth (Figure 3). Concentrations remain low until ~640 m depth where they increase to 7 mM. Methane concentrations up to 1.2 mM were measured between ~440 and ~640 m, consistent with the absence of sulfate. Ammonium sharply increases from 0.16 mM at the top of the core to 1.2 mM in 30 mbsf and then decreases to 0.5 mM at the bottom of the core. Total alkalinity exhibits a two-peak profile. One maximum of ~16 mM occurs around 20 mbsf. From there it decreases linearly down to 3 mM in 220 mbsf. Below this TA rises back to 13 mM in 375 mbsf and decreases again downcore back to 2 mM in 700 mbsf at the end of the record. Pore-water Ba^{2+} concentrations increase slightly from ~8 to ~25 µM from 0 to ~200 m depth, followed by much higher values, ranging from 25 to 440 µM, between ~200 m and ~640 m depth. Deeper than ~640 m, concentrations remain around 25 µM. Pore-water Li^{+} and Ca^{2+} concentrations increase with depth. Both have their lowest concentrations at the sediment surface (Li^{+} ~24 µM, Ca^{2+} ~10 mM). Lithium shows a broad concentration maximum of ~55 µM between ~300 and 550 m depth, a minimum of ~12 µM at ~560 m, and another increase towards the bottom of the core (~100 µM), Ca^{2+} increases to ~17 mM at ~220 m depth, displays minimum concentrations of ~14 mM between ~300 and 500 m depth, and increases again to ~30 mM towards the bottom of the core. Fe^{2+} has a maximum concentration of ~50 µM at 3.8 m depth and a peak of ~57 µM at 22 m depth (Figure 3). From there, it decreases to background

levels of <2 µM at 45 m depth where it stays for the remainder of the section. Some minor peaks up to 10 µM only occur between 45 and 150 m depth. Fe^{2+} increases to 4 µM in the deepest sample at ~700 m depth. Pore-water Mg^{2+} decreases from 50 to 25 mM over the upper 200 mbsf. Below this depth it increases slightly to 30 mM around 400 mbsf and decreases to 15 mM towards the end of the record. Pore-water Sr^{2+} is around 100 µM at the sediment surface and increases to 160 - 180 µM at 260 mbsf. It remains around these values down to 500 mbsf, and from there decreases slightly to 140 µM towards the bottom of the core.

The main chemical constituents of the sediments at Site U1417 are Si (av. 26.4 wt%) and Al (av. 8.4 wt%), with a Si/Al similar to average shale (Wedepohl, 1971, 1991). Deeper than ~350 m, Si contents fluctuate significantly and exhibit several peaks that mirror minima in Al (Figure 4). This results in a high Si/Al ratio. These peaks do not have equivalents in Zr or Zr/Al, indicating that Si enrichment is probably caused by biogenic diatomaceous productivity and not by enrichment of coarse siliciclastic material.

Total Fe contents display an average value of 5.7 wt%, but show excursions to much lower values below ~350 m, some of them anti-correlated with peaks in Si. These excursions are not visible in Fe/Al (Figure 5), indicating that Fe is not depleted but diluted by diatomaceous Fe-poor material. On average, 18.4 % of FeT resides in the FeHR fraction (Figure 5). Total S contents are generally low, averaging around 0.2 wt%, but two distinct peaks at ~570 m and ~680 m depth exceed 2 wt% (Figure 4). These maxima occur in depth intervals also exceeding 2 wt% pyrite-bound sulfur, indicating that S enrichments are related to iron sulfide precipitation/accumulation (Figure 5). Iron mono-sulfides are below detection limit in all samples analyzed.

Total organic carbon (TOC) contents are generally low (av. 0.5 wt%) with a few maxima at ~470 m (1.7 wt%), ~570 m (2.7 wt%) and ~680 m (1.8 wt%) depth (Figure 4).

Maximum Ba/Al ratios up to 1200 ($Ba/Al*10^4$) are observed at ~160 m, between ~350 and 425 m, and at ~640 m depth, and exceed the background levels of around 80-100 ($Ba/Al*10^4$) recorded throughout the entire core (Figure 6).

Calcium carbonate ($CaCO_3$) is below 2 wt% in most samples and shows 3 distinct peaks of 7 wt% at ~200 mbsf in the zone of sulfate depletion, 20 wt% at 340 mbsf and 40 % at 450 mbsf right above the zone of methane accumulation (Figure 6). The peak at 450 m represents a highly cemented layer of authigenic carbonate which was difficult to penetrate and only poorly recovered during drilling. Shipboard X-ray diffraction (XRD) analysis identified this indurated carbonate layer as well-sorted quartz-feldspar sand cemented by low-Mg calcite (Jaeger et al., 2014).

Pyrite $\delta^{34}S$ values are variable but generally negative (as low as -46‰) throughout the entire cored section. In contrast, at ~300 m and between ~560 and 620 m depth, $\delta^{34}S$ reaches maximum values of +60‰ (Figure 6).

Below 640 m (in the lower zone of sulfate enrichment), H- and O-indices are low (H-index ~30-50; O-index ~60-140) indicating a very low reactivity of organic matter (Figure 7; Childress, 2016).

4. Discussion

Based on sulfate and methane profiles, the core is divided into three distinctive diagenetic regimes: a) an upper zone defined by a decline in pore-water sulfate

concentrations down to ~220 mbsf followed by an interval of very low sulfate from ~220 to 440 mbsf; b) a zone of methane accumulation between ~440 and 640 m, referred to here as the methanogenic layer; and c) a zone where sulfate increases below a sediment depth of ~640 m (Figure 6). In the upper part of the record, diagenesis is or has been driven by electron acceptor supply from the overlying seawater. Below the methanogenic layer, a deep SMTZ is formed due to a deep source of sulfate and possibly other electron acceptors.

Diagenesis fuelled by diffusion of sulfate across the sediment-water interface (0-440 m)

The upper 200 m of the sediment succession at Site U1417 show a “concave-down” pore-water sulfate profile (Figure 3) and near-total sulfate depletion occurs at ~200 m. The minimum in sulfate is relatively deep compared to another deep-water site in the GOA (~75 m at Site U1418, Figure 1; Jaeger et al., 2014) but in the range of observed deep-sea SMTZ depths reported by Egger et al. (2018). These authors report an average SMTZ depth of 170 m below seafloor underlying a >3500 m water column. A reason for this deep sulfate penetration could be the absence of methane diffusing upwards beyond ~440 m sediment depth, hence no AOM-driven sulfate reduction occurs. This interpretation is supported by the concave-down shape of the sulfate profile, which indicates that organoclastic sulfate reduction accounts for most of the sulfate depletion in the upper ~200 m of sediment (Niewöhner et al., 1998; Kasten et al., 2003). According to Meister et al. (2013), the concave-down shaped sulfate profile also indicates that sufficient reactive OM is available to deplete sulfate.

Accordingly, the TOC profile shows a slight decrease over the top 200 mbsf, supporting OM degradation by organoclastic sulfate reduction.

Elevated pyrite contents at Site U1417 only occur at ~70 m depth in a single peak, supporting ongoing or past sulfate reduction leading to pyrite precipitation in this sediment layer (Figure 5). An explanation for this localized diagenetic feature cannot be provided, as the profiles of other sediment components, e.g. TOC or Si, do not show any anomalies that allow us to attribute a process. The current zone of diagenetic Fe reduction lies higher in the sediment succession (at ~4 m depth) as indicated by the Fe^{2+} pore-water profile (Figure 3).

The sediments below the sulfate reduction zone are dominated by a sediment interval of ~200 m thickness where sulfate and methane are both very low (~200 to 440 mbsf, sulfate <3 mM, methane <1.5 µM). In this interval, the TOC content reaches its lowest values throughout the entire record (~0.5 wt%, Figure 4). This relationship indicates that organoclastic sulfate reduction depleted the reactive OM pool, and the remaining OM is too inert to support significant methanogenesis in this sediment interval. At the more coast-proximal IODP Site U1418 no sulfate and methane free interval has been detected but an SMTZ has been reported in ~75 mbsf (Jaeger et al., 2014). This implies spatially variable OM deposition and degradation across the Surveyor Fan.

Despite the lack of a shallow SMTZ at Site U1417, two clusters of high Ba/Al ratios occur at ~160 m and between ~325 and 425 m, most likely resulting from past and/or ongoing authigenic barite precipitation following dissolution of barite deeper in the sediment (Figure 6). When pore-water sulfate is depleted to become undersaturated with respect to barite, sedimentary barite dissolves, and when upward diffusing

dissolved Ba meets sulfate re-precipitating authigenic barite can build diagenetic fronts just above the SMTZ. Such authigenic barite fronts can re-dissolve again when the SMTZ moves upwards (Von Breymann et al., 1992; Torres et al., 1996). The Ba/Al peaks at ~160 m depth do not coincide with peaks in Si or Si/Al and therefore are most likely not caused by higher biosiliceous export productivity (Gingele et al 1999). More likely, they indicate ongoing barite formation around the maximum sulfate penetration depth, since that they are situated above the zone where the pore-water is enriched in Ba^{2+} (Figure 6). In contrast, the peaks between ~325 and 425 m most likely formed at paleo-SMTZs and are currently dissolving, as indicated by elevated pore-water Ba^{2+} concentrations in these intervals, and parallel pyrite peaks and a $CaCO_3$ peak around 350 m sediment depth (Figure 6). Some coinciding enrichment in Si/Al suggests that initially higher deposition of biosiliceous material could have caused a higher initial biogenic barite in this zone, too (Gingele et al., 1999). Temporary preservation of barite within sulfate-free pore-waters has been explained by *in situ* transformation of barite into more stable barium carbonate, which would not change the observed bulk Ba/Al records (Riedinger et al., 2006). Nevertheless, the pore-water Ba^{2+} profile at Site U1417 shows that these deeper barite accumulations are presently being dissolved due to sulfate depletion (Figure 6), and therefore might represent transient features.

The methanogenic layer (440-640 m)

Below ~440 m, and extending down to ~640 m, pore-waters exhibit methane concentrations up to ~1.2 mM (Figure 3). The methane-enriched zone has markedly higher TOC contents (up to ~3 wt%) compared to the overlying section (~0.5 wt%),

supporting increased methane production related to higher amounts and/or reactivity of OM (Figure 4). Pore-water sulfate concentrations are very low throughout this entire interval, as expected for methane-rich sediments.

The top of the methanogenic interval is marked by a strongly cemented carbonate layer at 450 m depth (Figure 6) that was poorly recovered during drilling due to its high degree of induration within largely soft sediments, and only yielded one angular fragment (~3 cm in diameter) of low-Mg calcite (Jaeger et al., 2014). Such carbonate-cemented layers can form when an SMTZ remains within a specific sediment depth for longer periods of time (e.g. ~2.4 Ma in the Bering Sea according to Pierre et al., 2016; Wehrmann et al., 2016). Due to the higher alkalinity in SMTZs produced by AOM, authigenic carbonate minerals precipitate, including calcite ($CaCO_3$) with various amounts of Mg or pure dolomite ($CaMg(CO_3)_2$) (Hathaway and Degens, 1969; Middelburg et al., 1990; Pierre et al., 2016; Wehrmann et al., 2016). This type of cementation has been observed, for example, in sandy turbidite layers in the Bering Sea (Hein et al., 1979; Wehrmann et al., 2011).

To evaluate if the current methane or Ca fluxes into the carbonate layer would be sufficient to cement the entire original pore-space within the time of sediment deposition at Site U1417, simple calculations based on Fick's first law of diffusion were conducted:

Eq. 1: $$J_{sed} = \Phi * D_{sed} * dC/dx$$

where: J_{sed} = diffusive CH_4 flux in the sediment, Φ = sediment porosity, D_{sed} = CH_4 diffusion coefficient and dC/dx = CH_4 concentration gradient. An example calculation can be found in the appendix.

Based on a seawater diffusion coefficient for methane of $1.39*10^{-9}$ m^2 s^{-1} (Boudreau, 1997), measured pore-water composition and physical sediment parameters, we calculate a diffusive methane flux of 18.6 mM m^{-2} a^{-1}, resulting in a duration of <300 ka required to completely cement the original quartz-feldspar sand layer. With respect to the carbonate-cemented layer, the measured pore-water composition is sufficient for the precipitation of authigenic carbonate. Furthermore, the absolute measured methane concentrations are not fully representative for the concentrations in the sediments. Methane can dissipate due to pressure release during core recovery, in particular in the deeper cores that were recovered using rotary drilling. Thus, the calculation might underestimate the current methane availability. The profile of pore-water Mg^{2+} exhibits broad maxima between ~300 and ~500 mbsf. This could indicate lateral inflow of ions necessary for carbonate formation. Interestingly, this pattern is not observed in Ca^{2+} which is the main cation-constituent of the low-Mg-calcite found in these layers (Jaeger et al., 2014).

Similar carbonate-rich, cemented intervals have been reported at the same depth interval at DSDP Site 178, approximately 1.5 km from Site U1417 (Kulm and Von Huene, 1973). This correlation indicates that carbonate cementation of otherwise permeable sediment layers in the GOA might be a spatially extended phenomenon.

A striking observation at U1417 is the relatively abrupt decrease of methane concentrations at 440 mbsf without the existence of an SMTZ. One possible reason for the methane not diffusing into the overlying sediments could be the installation of a physical barrier by the authigenic carbonate layers. The diffusive profiles of other pore-water constituents, however, appear unaffected across this sediment interval (e.g. NH_4, Figure 3), and small amounts of methane occur above the carbonate layer at 450 mbsf. Hence, the carbonate layer does not seem to be acting as a diffusive

barrier to gases and ions dissolved in the pore-water. An alternative explanation could be the oxidation of methane by small amounts of sulfate above 440 mbsf. As indicated by Ba/Al peaks and elevated pore-water Ba^{2+} and Sr^{2+} concentrations, barite dissolution is occurring in the sediment interval above 450 mbsf, and this process would release minor amounts of sulfate to the pore-waters which could drive AOM. We therefore propose a zone of cryptic AOM driven by the release of sulfate from dissolving barite in 375-425 mbsf. This process was proposed earlier by Treude et al. (2014). Sulfate concentrations in this sediment interval do not differ from those in the methanogenic zone, probably because the excess sulfate is balanced by AOM immediately. Dissolved Ba^{2+} concentrations in this zone reach values of up to 400 µM – the same order of magnitude as average measured methane concentrations in the methanogenic zone (in average ~500 µM in the methanogenic layer). One mole barite provides one mole of Ba^{2+} and one mole of sulfate to the pore-water, and one mole of sulfate is required to oxidize one mole of methane. Thus, the observed concentrations of Ba^{2+} and sulfate imply that barite dissolution is sufficient for total methane consumption above 440 mbsf. In support of this hypothesis, the alkalinity profile (Figure 3) indicates that AOM is occurring at present. Total alkalinity exhibits a second peak of 12 mM TA centered around 375 mbsf, coinciding with an enrichment in pore-water Ba^{2+}. Anaerobic oxidation of methane releases 2 moles of total alkalinity per mole of methane into the pore-water according to the reaction:

$$CH_4 + SO_4^{2-} \rightarrow HS^- + HCO_3^- + H_2O$$

Hence, this alkalinity peak is indicative of considerable AOM in this zone. We therefore suggest that carbonate cementation acting as diffusive barrier for methane flux into the overlying pore-waters is an unlikely explanation and that a cryptic sulfate release, probably driven by dissolving barites limits methane diffusion into overlying

sediments. This cryptic process could also have caused the authigenic carbonate cementation.

The sharp boundary between methane-bearing and methane-free sediments at Site U1417 further suggests that significant methanogenesis is only occurring below 440 mbsf where sufficient reactive OM is available.

The sediment Ba/Al ratio in the methanogenic layer below 440 mbsf is consistently low and reaches detrital background levels (Condie, 1993) whereas dissolved Ba^{2+} is high, indicating long-lasting sulfate-depleted conditions and near-quantitative dissolution of barite (Figure 6). The Fe-S/FeHR ratio is higher in the methanogenic layer (peak values of 0.2 - 0.6) than above it, reaching a maximum at ~575 m (Figure 5). The elevated Fe-S/FeHR ratio most likely reflects the transformation of iron (oxyhydr)oxides into pyrite within a paleo-SMTZ (Canfield et al., 1992; Raiswell and Canfield, 1998). The dissolved Fe required for Fe-S precipitation could be provided by Fe-oxide reduction coupled to methane oxidation as proposed by Egger et al. (2017). However, the pore-water Fe content in the methanogenic layer is very low, indicating that this process is no longer operational (Figure 3).

High values of FeHR/FeT co-occur with the Fe-S/FeHR enrichments, most likely related to higher inputs of reactive Fe minerals to Site U1417. This interpretation is in agreement with higher amounts/reactivity of TOC in the methanogenic layer. Excess terrestrial Fe (mainly as (oxyhydr)oxides that contribute to the FeHR pool) delivered to the GOA should have fertilized primary productivity in this part of the iron-limited North Pacific and enhanced marine OM export to the seafloor (e.g. Martin, 1990). Additionally, diagenetic mobilization of iron (oxyhydr)oxides could have led to the enrichment of FeHR in specific sediment intervals where changes in sedimentation

rate would have led to the fixation of the oxic-suboxic redox boundary, producing diagenetic accumulations of Fe (oxyhydr)oxides (Kasten et al., 1998).

Deep sulfate reservoir and inverse SMTZ (below 640 m)

The deepest 60 m of the sediment record (below 640 m depth) are characterized by a downcore increase in pore-water sulfate. Between the methanogenic layer and this deep sulfate enrichment lies an “inverse” SMTZ which, in contrast to a conventional SMTZ (e.g. Martens and Berner, 1977; Niewöhner et al., 1997), is characterized by methane diffusing down, and sulfate diffusing up.

This inverse SMTZ is associated with the highest Ba/Al peak of the entire U1417 record, likely representing a zone of long lasting and still ongoing authigenic barite formation (Figure 6). Therefore, an active SMTZ with an electron acceptor supply from below can be assumed. Pore-water Li^+ and Ca^{2+} concentrations increase towards the base of the sediment succession, providing evidence for chemical interaction between sedimentary pore-waters and the oceanic crust (Figure 3). The Li^+ and Ca^{2+} ions are leached out of the basaltic basement and diffuse into the pore-waters of the overlying sediments. This trend indicates that the pool of sulfate-rich water is in contact with, or even circulating through, the oceanic basement (Gieskes et al., 1982).

Deep SMTZs with an electron acceptor supply from the bottom of the sediment column have been reported previously from other ocean regions. Sites where this phenomenon has been described and studied generally fall into one of five categories:

(1) Seawater can enter deep sediment layers or the oceanic basement where these layers crop out at the seafloor, and circulation through the subsurface can be driven by thermal gradients. Oceanic spreading centers are common settings for this type of fluid circulation within sediments and the underlying oceanic crust. Here, thermal energy from the hot crust drives fluid flow, and the thin sediment cover supports seawater circulation into and out of the crust (Elderfield et al., 1999; Engelen et al., 2008; Kuhn et al., 2017). Seamount flanks play an even greater role in recharging deep aquifers at the base of the sediment cover, with reported fluid flow over distances of up to 50 km at the Juan de Fuca Ridge (ODP Leg 168; Fisher et al., 2003a, 2003b; Hutnak et al., 2006). Deep sulfate enrichments observed at ODP Sites 1225 and 1226 in the open Pacific Ocean off Peru could also be attributed to this hydrological regime, but since sulfate is not depleted throughout the sediment column at these sites, no inverse SMTZs are installed (D'Hondt et al., 2003).

(2) At accretionary wedges above subduction zones, compressional dewatering of the accreted and subducting sediments leads to an active regime of subsurface fluid flow. This has been observed, for example, in the Nankai Trough off Japan (e.g. Torres et al., 2015). A combination of spreading center and accretionary wedge fluid flow has been observed at the Chile Triple Junction, where a spreading center is being subducted (ODP Leg 141; e.g. Agar and Prior, 1995).

(3) Along continental margins, contributions of terrestrial groundwater can be introduced into marine sediment layers and install aquifers with a chemistry deviating from the marine-derived pore-water. For the Southeast Greenland Margin, contributions of meteoric water derived from the coast of Greenland were suggested as an explanation for the observed pore-water profiles. These pore-waters also react

with volcanic ash layers, further modifying their chemistry (Larsen et al., 1994; Gieskes et al., 1998). Most recently, an expansive aquifer system was discovered with geophysical methods off the East Coast of the USA (Gustafson et al., 2019).

(4) Sulfate supply from buried evaporitic deposits does not require active fluid flow but relies on diffusion alone. Sulfate can be provided by dissolution of deeper gypsum- or anhydrite-rich layers and can diffuse into the overlying sediment column. Prominent examples are several drill sites in the Mediterranean (ODP Expedition 160; Böttcher et al., 1998), where thick and extensive evaporite layers formed during the Messinian Salinity Crisis (Hsü et al., 1973; Hsü et al., 1977). This process also plays a role at ODP Site 1229 at the Peru margin (Leg 201; D'Hondt et al., 2003).

(5) Sulfate rich pore-waters could have been buried by sharp increases in sedimentation rates. This scenario was proposed by Brumsack et al. (1992) in the Sea of Japan (ODP Sites 796 and 797). The authors state that very low sedimentation rates allowed seawater sulfate to penetrate deeply into the sediments. Sulfate diffusion rates from the overlying water column strongly exceeded the rate of sulfate reduction within the sediments, preventing significant sulfate depletion in the pore-waters. A subsequent rise in sedimentation rates led to a separation of the seawater sulfate from the deep pool. This explanation has been proposed for deep, sulfate-enriched pore-waters at ODP Site 898 (ODP Leg 149) on the Iberia abyssal plain (Meyers and Shaw., 1996; Meyers et al., 1996). A situation where, due to low sedimentation rates and organic matter reactivity, electron acceptors diffuse deep into the sediments without being depleted can currently be seen in the South Pacific Gyre (D'Hondt et al., 2009; Fischer et al., 2009).

These documented scenarios of deep sulfate supply may not be fully applicable or satisfactory to explain the geochemical observations at Site U1417. The study site

lies on a subducting plate, but is presently ~75 km away from the subduction zone. Therefore, it is unlikely that subduction-related dewatering of accreting or subducting sediments accounts for the sub-seafloor hydrology at Site U1417. The transport of terrestrial groundwater to the site across the subduction zone is also an unrealistic scenario, since any groundwater would be confined to the continental shelf and upper slope. In this area of the North Pacific, no evaporite deposits have been reported and it is highly unlikely that they formed in this open-marine, high-latitude environment in the past. The oceanic basement at this site is buried beneath ~800 m of sediment, which is a fairly thick sediment cover compared to seamount or ridge flanks. In addition, minimal crustal heat flow can be expected in the GOA, with an oceanic basement age as old as ~43 million years (Gee and Kent, 2007) and overlying pillow basalt ages of ~26 Ma (this study). Seamounts as a source for the deep sulfate-rich water are a more likely explanation. The Giacomini Guyot and Kodiak Seamount are close to Site U1417 (Turner et al., 1973) and could provide entry points for seawater. However, at distances of 131 km (Kodiak) and 73 km (Giacomini), both are farther from the site than the 50 km reported by Fisher et al. (2003a, 2003b) and Hutnak et al. (2006).

Another possiblescenario is that the sulfate pool at U1417 was buried during deposition of the deepest sediment layers in the Miocene and has since then not been consumed completely by bacterial sulfate reduction. Due to low organic matter reactivity in these deep Miocene sediments, sulfate may not have been fully reduced until today. Indeed, the lowest ~100 m of the sediment succession at Site U1417 (615+ m) were deposited over a period of more than 8 Ma at low sedimentation rates (1 cm ka^{-1}). An increase in sedimentation rates from 1 cm ka^{-1} to 6 cm ka^{-1} occurred

around 8 Ma (Jaeger et al., 2014), which is represented today by the sediment depth of ~615 m, shortly above the current inverse SMTZ in ~640 m depth.

Besides the hypothesis of an old, residual sulfate pool preserved at depth at Site U1417, there is another explanation involving the active delivery of relatively "young" seawater sulfate to the base of the sediment succession. In the northern parts of the GOA, large-scale tectonic processes lead to plate bending as the Pacific Plate approaches the Aleutian subduction zone (Masson, 1991; Reece et al., 2013). This bending could have generated new hydrological pathways near the study site through the formation of plate bending faults. Extension due to plate bending generates an array of sub-parallel normal faults that are observed to offset from seafloor through the sediment sequence and the top of the oceanic crust (Reece et al., 2013). Such faults have previously been reported as an important process in hydrating subducted tectonic plates and exporting water into the mantle (e.g. Emry and Wiens, 2015; Naif et al., 2015; Cai et al., 2018; Shillington, 2018). Probably, in the GOA they could act as pathways for seawater supplying the observed deep sulfate pool at U1417. Based on existing seismic data within the GOA, plate bending faults are present within ~250 km of the Aleutian Trench (Figure 2). These faults occur near Site U1417 and for up to ~176 km to the southeast parallel to the direction of the Pacific Plate motion.

Deep buried sulfate pool versus actively flowing deep aquifer

In the following section we will attempt to distinguish between the possible origins of deep sulfate enrichment at Site U1417: a deep buried sulfate pool or an actively

flowing deep aquifer, either recharged through plate bending faults or from seamount flanks.

In this context, the analysis of S isotopes can provide useful information on the source of deep pore-water sulfate at Site U1417. In marine sediments, bacterial sulfate reduction is accompanied by S isotope fractionation. Sulfate containing the lighter ^{32}S isotope is preferably reduced to sulfide by bacteria and isotopically lighter (i.e. depleted in ^{34}S) pyrite is precipitated compared to the parental seawater sulfate. Conversely, the remaining sulfate-S becomes isotopically heavier, i.e. enriched in ^{34}S (Hartmann and Nielsen, 1969; Jorgensen, 1979; Strauss, 1997, 1999; Canfield, 2001). Sulfur isotopic fractionation associated with bacterial sulfate reduction can be as high as 70‰ (Rudnicki et al., 2001; Wortmann et al., 2001; Ono, 2008; Sim et al., 2011). Pyrites depleted in ^{34}S are generally only produced when an unlimited supply of sulfate is available for sulfate reduction (open system) and other environmental parameters (e.g. type and availability of OM as electron donor) remain stable (e.g. Leavitt, 2014). In contrast, bacterial sulfate reduction occurring under sulfate-limited conditions (closed system) leads to a progressive decrease of the sulfate pool, and its S isotopic composition of the formed pyrites becomes progressively more enriched in ^{34}S (i.e. isotopically heavier; Canfield, 2001). Böttcher et al. (2006) showed that deep, tectonically sourced pools of sulfate have often already undergone sulfate reduction, leading to a sulfate-S enriched in the heavy isotopes. In our scenario involving an old buried pool of sulfate depleted to ~7 mM, even higher enrichments in the heavy isotope can be expected.

Pyrite-S isotopes below 640 m depth are, however, strongly negative (-10‰ to -30‰, Figure 6), indicating an open system with limited sulfate depletion. About 40% of the total sedimentary Fe (up to 80% of the highly reactive Fe) are pyritized in samples

with high FeHR values (Figure 5). In samples below 640 m, there is a near 1:1 relationship between FeHR/Fetot and Fe-S/FeHR (not shown). This finding indicates that samples with high FeHR contents are nearly completely pyritized. This high degree of pyritization suggests that, at present, no further authigenic pyrite precipitation takes place. The light S-isotopy of the pyrites is a strong indicator that the pyrites have either precipitated diagenetically before the installation of the deep sulfate pool, or under unlimited sulfate supply, either shortly after the establishment of the sulfate-rich buried pool or progressively under an unrestricted supply of “fresh”, sulfate which had not undergone significant sulfate reduction. If pyritization was already completed before either the deep sulfate pool was cut off or the deep aquifer was installed, the S isotopic composition of the pyrite would reflect the geochemical conditions before this event, as no further pyrite precipitation could have occurred due to the lack of excess FeHR. Since we have no further means to constrain the point in time at which pyritization was completed, nor the time period over which the pyrite-S isotope signatures were generated, further investigations are necessary to reveal the origin of the deep sulfate pool.

A pronounced Ba/Al peak is found at the center of the current inverse SMTZ, indicating ongoing barite precipitation (Figure 6). The absence of Ba/Al peaks farther below or above suggests that this discrete zone of barite precipitation must have been fixed within the current sediment interval. It also indicates that either no diagenetic barite ever formed above or below this layer, or that barite precipitated above has been dissolved. In contrast, pyrite-rich layers occur above and below the current SMTZ (Figure 5). At ~570 m depth, a layer with an Fe-S/FeHR ratio of 0.6 is found, and pyrite-S isotopes are positive (up to +50‰; Figure 6). This result could indicate that the position of the pyrite enrichments marks the previous position of the

SMTZ.

The strongly enriched $\delta^{34}S$ of pyrite at ~570 m depth indicates that it formed during a phase of severe sulfate limitation. This enrichment could provide support for the hypothesis of a deep residual sulfate pool that was disconnected from overlying seawater sulfate in the past. In a discrete sediment interval, a temporary increase in sulfate reduction rates, for example due to the presence of reactive OM, could have generated sulfate-limited conditions and accumulation of isotopically heavy pyrite. Indeed, higher TOC contents can still be found in the respective sediment intervals. If strongly increased sulfate reduction rates were short-lived, this could have consumed sulfate in relatively shallow sediments while leaving a residual sulfate pool still existing in deeper sediment layers unaffected.

To assess the hypothesis of a deep residual sulfate pool that persisted within the deeply buried Miocene deposits at Site U1417, it is critical to know the nature of the organic material below 640 mbsf. If the organic material was easily degradable by microorganisms, it should have been remineralized by sulfate reduction over the last millions of years since its burial. If the organic material, in contrast, was highly refractory, it could have persisted in the Miocene sediments without supporting significant microbial sulfate reduction. Therefore, the reactivity of the organic matter within the sulfate-containing deep sediments at Site U1417 can indirectly provide useful information about the relative age of the deep sulfate pool.

At Site U1417 below ~600 mbsf, the sediments contain relatively high amounts of organic matter (up to 2 wt% TOC; Figure 4). An HI of 30 – 50 mg HC/g TOC and an oxygen index (OI) of 60 – 140 mg CO_2/g TOC in the deepest sediment interval indicates that all organic matter here is kerogen type IV (Figure 7), an unreactive material that is generally associated with coal-related carbon and can be considered

an inert end-member of detrital organic matter that has experienced significant thermal oxidation, biological degradation, and/or sedimentary recycling (Vandenbroucke and Largeau, 2007; Figure 7). These values suggest that the remaining organic matter in the deepest deposits at U1417 is predominantly unreactive. Consequently, it is conceivable that microbes could not use this organic material for dissimilatory sulfate reduction, implying that a Miocene buried sulfate pool could have been preserved within these deep sediment layers. However, as there is a contact between the sulfate- and the methane-rich zones, the question arises why the deep sulfate did not get reduced by AOM in the inverse SMTZ. To assess this question, we calculated the time it would take to deplete a sulfate pool at seawater sulfate concentration (28 mM) in these sediments by AOM. This calculation can again be done using Fick's first law of diffusion (Eq. 1; example in appendix). With a seawater diffusion coefficient for sulfate of $9.95*10^{-10}$ m^2 s^{-1} (Boudreau, 1997) and based on the current concentration gradient, we calculate a diffusive flux of 672 µmol m^{-2} a^{-1} for sulfate. With this flux it would take ~3 Ma to consume the deep sulfate pool by AOM, a time period much shorter than the time since the Miocene when this deep sulfate pool would have been originally buried. Using the current sulfate flux as a benchmark, it can henceforth be concluded that having preserved an old, deeply buried sulfate pool at Site U1417 is an unrealistic scenario and that the sulfate-rich water must be replenished by another process. As stated earlier, we suggest that a tectonic driver was responsible for the installation of the deep sulfate-enriched aquifer.

To distinguish between possible tectonic drivers, Fick's first law of diffusion can be used to estimate the time it has taken, under steady state conditions, to accumulate the Ba peak at 644 m depth (assuming it is exclusively composed of authigenic

barite at the present deep SMTZ). This calculation has to be based on the assumptions that the Ba layer formed within the same depth interval and that no dissolution and re-precipitation occurred. Peak dissolution would have occurred when the SMTZ moved and barite precipitation would have occurred in other sediment intervals as well. But in this case, relict Ba peaks should still be observable in these sediment intervals. As no relict Ba peaks can be observed above or below the main Ba peak, the assumption that the center of Ba formation has constantly been stable within the same sediment interval is plausible.

The calculated time estimate can be compared to the onset of plate bending at Site U1417 and the eruption time of nearby seamounts. Based on seismic data within the Gulf of Alaska, Pacific plate bending faults are present within ~250 km distance of the Aleutian Trench. Relative to Site U1417, these faults occur up to ~176 km to the SE along the Pacific Plate vector. Using MORVEL2010 (DeMets et al., 2010) where the Pacific Plate at this location is moving at ~45 mm a^{-1} at a NW angle of -315.19°, we calculate that Site U1417 passed through this location of expected plate bending fault onset (~176 km to SE) ~3.9 Ma ago and still lies within a zone of plate bending faults today (Figure 2). The closest seamounts, Giacomini and Kodiak, which could also have installed new hydrological pathways through the sediment, erupted at 19.9 ± 1.0 Ma and 22.6 ± 1.1 Ma, respectively (Turner et al., 1973), and the basalt layer at the basement of DSDP Site 178 (collocated with IODP Site 1417) was dated to 25.80 ± 0.36 Ma (see above).

Equation 1 is applied in this case with a seawater diffusion coefficient for Ba^{2+} of 5.25 $*10^{-10}$ m^2s^{-1} (Boudreau, 1997) and based on the currently observed Ba^{2+} concentration gradient. Example calculations can be found in the appendix. The calculation was carried out using several estimates for the thickness of the Ba-

enriched layer, as the low sampling resolution in these deep layers of the drill core makes it difficult to precisely constrain the amount of accumulated Ba at the SMTZ. The chosen combination of values and the derived calculations as well as an example calculation are presented in the Appendix. We calculate a diffusive downward flux of $5.92*10^{-5}$ moles$*m^{-2}*a^{-1}$ to cause the accumulation of the Ba peak. The Ba-enriched layer has an excess Ba enrichment of 0.73 wt% compared to background Ba concentrations (Wedepohl, 1971, 1991). Using these numbers, we calculate accumulation times of ~300 ka if the Ba-rich sediment interval spans 50 cm (minimum estimate based on the distance between the two Ba-rich samples) to ~6.1 Ma assuming a constant Ba enrichment of 0.73 wt % over a 10 m sediment interval. Given the low sample resolution, even higher values for the Ba-rich sediment volume would be possible. However, the amounts of Ba required for even higher authigenic barite enrichments would imply unrealistically high primary barite deposition rates over the sedimentation history at Site U1417 (Pfeifer et al., 2001).

These time estimates based on authigenic Ba accumulations are most similar to the calculated time of initiation of the plate bending faults, while the eruptions of the closest seamounts occurred much further in the past. We therefore suggest that plate bending delivered sulfate-bearing waters to the deep reservoir at the bottom of Site U1417. This hypothesis is further supported by clearly imaged plate bending faults in the vicinity of Site U1417 (Figure 2). The offset in time between our geochemistry- and tectonic-based estimates for the first appearance of this deep aquifer could be caused by variable fluxes of Ba^{2+} over time. Alternatively, a gradual increase in the effectiveness of plate bending normal faults as fluid conduits could be the reason, such as through the process of increasing fault gouge over time, as they approach the subduction zone. Furthermore, newly developed faults do not

necessarily act as an instantaneous connection between the seawater and the deep sediment layers, and seawater penetration to the base of the sediment column was likely retarded in the early stages of fault installation. Within the large uncertainties of our calculations, however, we conclude that the accumulation time for the authigenic Ba layer lies within the same order of magnitude as the onset of plate bending at Site U1417, and we propose that both processes are connected.

Comparison with DSDP Site 178 (Leg 18)

IODP Site U1417 is a re-drill (offset by ~1.5 km) of DSDP Site 178 (Kulm and Von Huene, 1973; Jaeger et al., 2014). In contrast to Site U1417, basement has been reached during drilling at Site 178. It is therefore imperative to compare geochemical profiles from Site U1417 to the profiles from Site 178. Figure 8 shows TOC and pore-water results from Site 178 alongside the same data from Site U1417. The depth scales might not be entirely corresponding because of the spatial distance between both sites, however, the matching profiles of Ca, Mg and sulfate in the upper part of the record indicate that comparability is sufficient for the purpose of this study.

The sulfate profile at Site 178 looks similar to the one at Site U1417 in the upper 200 mbsf, implying that the same processes govern sulfate reduction and organic matter degradation at both sites. Below 200 m, sulfate at Site 178 is higher than in the same interval at Site U1417. Unfortunately, methane has not been analyzed at Site 178, but the sulfate concentrations suggest that methanogenesis only occurs below 440 mbsf. The similar shapes of the TOC profiles further suggest that the processes of OM degradation are similar at both sites. A striking observation is that the lower sulfate pool at Site U1417 is not observed at Site 178. Sulfate only increases slightly

towards the basement. In contrast, dissolved Ba^{2+} is much higher in the lowest interval. These higher pore-water Ba^{2+} concentrations at Site 178 have originally been attributed to higher biogenic Ba deposition (Waterman et al., 1973). This could also explain the primary origin of the Ba which is diagenetically enriched at Site U1417. The differing pore-water sulfate profiles indicate that the process of sulfate enrichment at Site U1417 potentially is a spatially limited phenomenon. In the context of the processes described above, this observation challenges the hypothesis of an outcrop-to-outcrop flux between two seamounts, because this sort of flux should affect the entire seafloor between these outcrops. As sedimentation rates and organic matter flux are also similar at both sites, a deep buried pool of sulfate should therefore most likely also appear at both sites. Plate bending fault-derived sulfate could, however, produce spatially variable diagenetic signals depending on the distance of the site from the fault.

The cumulative evidence from geochemical observations, calculations of diffusive fluxes and mineral accumulations and the variation of geochemical profiles between the neighboring sites U1417 and 178 is mostly in accordance with plate bending faults as a way of recharging a deep aquifer and providing sulfate to the deeper sediments in the Gulf of Alaska (Figure 9). Plate bending has previously been reported as an important process in hydrating subducted tectonic plates and in exporting water into the mantle (e.g. Emry and Wiens, 2015; Naif et al., 2015; Cai et al., 2018; Shillington, 2018). For the first time, we are proposing a link of this process with low temperature biogeochemical element cycling in marine sediments. With respect to crustal hydration and water export into the Earth's mantle in subduction zones, plate bending has been assigned similar importance as water circulation at seamount flanks and along mid-oceanic ridges (Cai et al., 2018; Shillington, 2018). It

is therefore plausible that it has equally far-reaching effects on sediment biogeochemistry.

5. Conclusions

At IODP Site U1417 in the GOA, inorganic and organic geochemical data unravel the complex evolution of early diagenetic processes with clear evidence for non-steady state conditions and a distinct deviation from the canonical catabolic sequence. We present two key observations. First, a spatial separation of the sulfate reduction and methane oxidation zones caused by methane consumption with sulfate which is released from dissolving barites. Second, an enrichment of sulfate is observed in the deeper sediment layers, well below a zone of sulfate depletion and a methane generating layer. The sulfate-rich water in the deep subsurface causes an inverse diagenetic zonation close to the sediment-basement interface. We propose that a deep aquifer, recharged through extensional faults generated by plate bending, provides this sulfate-containing seawater. Based on the findings at Site U1417, the area of the global seafloor where deep aquifers and multiple sulfate-methane transition zones may exist has to be expanded to include portions of the seafloor which are affected by plate bending. This result can have far-reaching implications for deep biosphere biomass estimations and the global carbon and sulfur cycles.

6. Acknowledgements

The authors sincerely thank the Captain, Crew, and Scientific Party of the Joides Resolution for their hard work to realize IODP Expedition 341. Further thanks go to Phillip Green (Newcastle), Artur Fugmann (Münster), as well as Carola Lehners and

Eleonore Gründken (Oldenburg) for supporting the analytical work. This research was funded by the Natural Environment Research Council (NERC), the European Consortium for Ocean Research Drilling (ECORD), UK IODP, the School of Civil Engineering and Geosciences at Newcastle University, NSF award 1434656 to Dr. Benowitz, NSF award 1435121 to Dr. Gulick, and NSF award ### to Dr. Jaeger

This is UTIG Contribution #XXXX.

Literature

Agar, S.M., Prior, D.J., 1995. Faulting and Fluid Flow in Accreted Sediments: Hole 863B, Chile Triple Junction, in: Proceedings of the Ocean Drilling Program, 141 Scientific Results. https://doi.org/10.2973/odp.proc.sr.141.016.1995

Benowitz, J.A., Layer, P.W., Vanlaningham, S., 2014. Persistent long-term (c. 24 Ma) exhumation in the Eastern Alaska Range constrained by stacked thermochronology. Geological Society, London, Special Publications, 378, 225–243. https://doi.org/10.1144/SP378.12

Boetius, A., Ravenschlag, K., Schubert, C.J., Rickert, D., Widdel, F., Gieseke, A., Amann, R., Jørgensen, B.B., Witte, U., Pfannkuche, O., 2000. A marine microbial consortium apparently mediating anaerobic oxidation of methane. Nature 407, 623–626. https://doi.org/10.1038/35036572

Böttcher, M., Brumsack, H.-J., de Lange, G., 1998. Sulfate Reduction and Related Stable Isotope (34S, 18O) Variations in Interstitial Waters From the Eastern Mediterranean. . Proceedings of the Ocean Drilling Program, Scientific Results 160, 365–373.

Böttcher, M.E., Ferdelman, T.G., Jørgensen, B.B., Blake, R.E., Surkov, A.V., Claypool, G.E., 2006. Sulfur Isotope Fractionation by the Deep Biosphere within Sediments of the Eastern Equatorial Pacific and Peru Margin, in: Proceedings of the Ocean Drilling Program, 201 Scientific Results. https://doi.org/10.2973/odp.proc.sr.201.109.2006

Boudreau, B.P., 1997. Diagenetic models and their implementation. Modelling transport and reactions in aquatic sediments, Springer, New York. https://doi.org/0.l007/97S-3-642-60421-S

Bowles, M.W., Mogolĺon, J.M., Kasten, S., Zabel, M., Hinrichs, K.U., 2014. Global rates of marine sulfate reduction and implications for sub-sea-floor metabolic activities. Science, 344, 889–891. https://doi.org/10.1126/science.1249213

Brumsack, H. J., Zuleger, E., Gohn, E., Murray, R. W., 1992. 36. Stable and Radiogenic Isotopes in Pore Waters from Leg 127, Japan Sea. . Proceedings of the Ocean Drilling Program, Scientific Results 127/128, Pt. 1.

Cai, C., Wiens, D.A., Shen, W., Eimer, M., 2018. Water input into the Mariana subduction zone estimated from ocean-bottom seismic data. Nature 563, 389-392. https://doi.org/10.1038/s41586-018-0655-4

Canfield D.E., 2001. Biogeochemistry of sulfur isotopes. Reviews in Mineralogy and Geochemistry 43, 607-636.

Canfield, D.E., Raiswell, R., Westrich, J.T., Reaves, C.M., Berner, R.A., 1986. The use of chromium reduction in the analysis of reduced inorganic sulfur in sediments and shales. Chemical Geology 54, 149–155. https://doi.org/10.1016/0009-2541(86)90078-1

Canfield, D.E., Raiswell, R., Bottrell, S., 1992. The reactivity of sedimentary iron minerals toward sulfide. American Journal of Science 292, 659–683. https://doi.org/10.2475/ajs.292.9.659

Childress, L. B., 2016. The Active Margin Carbon Cycle: Influences of Climate and Tectonics in Variable Spatial and Temporal Records. Earth and Planetary Sciences. Evanston, IL: Northwestern University. ProQuest Number: 10117251

Condie, K.C., 1993. Chemical composition and evolution of the upper continental crust: Contrasting results from surface samples and shales. Chemical Geology 104, 1–37. https://doi.org/10.1016/0009-2541(93)90140-E

Contreras, S., Meister, P., Liu, B., Prieto-Mollar, X., Hinrichs, K.-U., Khalili, A., Ferdelman, T.G., Kuypers, M.M.M., Jorgensen, B.B., 2013. Cyclic 100-ka (glacial-interglacial) migration of subseafloor redox zonation on the Peruvian shelf. Proceedings of the National Academy of Sciences 110, 18098–18103. https://doi.org/10.1073/pnas.1305981110

D'Hondt, S. L., Jorgensen, B.B., Miller, D.J., and Shipboard Scientific Party, 2003. Proceedings of the Ocean Drilling Program, 201. Initial Reports. Ocean Drilling Program. https://doi.org/10.2973/odp.proc.ir.201.2003

D'Hondt, S., Jørgensen, B.B., Miller, D.J., Batzke, A., Blake, R., Cragg, B.A., Cypionka, H., Dickens, G.R., Ferdelman, T., Hinrichs, K.U., Holm, N.G., Mitterer, R., Spivack, A., Wang, G., Bekins, B., Engelen, B., Ford, K., Gettemy, G., Rutherford, S.D., Sass, H., Skilbeck, C.G., Aiello, I.W., Guèrin, G., House, C.H., Inagaki, F., Meister, P., Naehr, T., Niitsuma, S., Parkes, R.J., Schippers, A., Smith, D.C., Teske, A., Wiegel, J., Padilla, C.N., Acosta, J.L.S., 2004. Distributions of microbial activities in deep subseafloor sediments. Science. 306, 2216–2221. https://doi.org/10.1126/science.1101155

D'Hondt, S., Spivack, A.J., Pockalny, R., Ferdelman, T.G., Fischer, J.P., Kallmeyer, J., Abrams, L.J., Smith, D.C., Graham, D., Hasiuk, F., Schrum, H., Stancin, A.M., 2009. Subseafloor sedimentary life in the South Pacific Gyre. Proceedings of the National Academy of Sciences 106, 11651–11656. https://doi.org/10.1073/pnas.0811793106

DeLong, E.F., 2004. Microbial life breathes deep. Science 306, 2198-200 https://doi.org/10.1126/science.1107241

DeMets, C., Gordon, R.G., Argus, D.F., 2010. Geologically current plate motions. Geophysical Journal International 101, 425-478. https://doi.org/10.1111/j.1365-246X.2009.04491.x

Dickens, G.R., 2001. Sulfate profiles and barium fronts in sediment on the Blake Ridge: Present and past methane fluxes through a large as hydrate reservoir. Geochimica et Cosmochimica Acta 65, 529–543. https://doi.org/10.1016/S0016-7037(00)00556-1

Egger, M., Hagens, M., Sapart, C.J., Dijkstra, N., van Helmond, N.A.G.M., Mogollón, J.M., Risgaard-Petersen, N., van der Veen, C., Kasten, S., Riedinger, N., Böttcher, M.E., Röckmann, T., Jørgensen, B.B., Slomp, C.P., 2017. Iron oxide reduction in methane-rich deep Baltic Sea sediments. Geochimica et Cosmochimica Acta 207, 256–276. https://doi.org/10.1016/j.gca.2017.03.019

Egger, M., Riedinger, N., Mogollón, J.M., Jørgensen, B.B., 2018. Global diffusive fluxes of methane in marine sediments. Nature Geoscience 11, 421-425. https://doi.org/10.1038/s41561-018-0122-8

Elderfield, H., Wheat, C.G., Mottl, M.J., Monnin, C., Spiro, B., 1999. Fluid and geochemical transport through oceanic crust: A transect across the eastern flank of the Juan de Fuca Ridge. Earth and Planetary Science Letters 172, 151–165. https://doi.org/10.1016/S0012-821X(99)00191-0

Emry, E.L., Wiens, D.A., 2015. Incoming plate faulting in the Northern and Western Pacific and implications for subduction zone water budgets. Earth and Planetary Science Letters. 414, 176–186. https://doi.org/10.1016/j.epsl.2014.12.042

Engelen, B., Ziegelmüller, K., Wolf, L., Köpke, B., Gittel, A., Cypionka, H., Treude, T., Nakagawa, S., Inagaki, F., Lever, M.A., Steinsbu, B.O., 2008. Fluids from the oceanic crust support microbial activities within the deep biosphere. Geomicrobiology Journal 25, 56–66. https://doi.org/10.1080/01490450701829006

Fischer, J.P., Ferdelman, T.G., D'Hondt, S., Røy, H., Wenzhöfer, F., 2009. Oxygen penetration deep into the sediment of the south pacific gyre. Biogeosciences 6, 1467–1478. https://doi.org/10.5194/bg-6-1467-2009

Fisher, A.T., Davis, E.E., Hutnak, M., Spiess, V., Zühlsdorff, L., Cherkaoui, A., Christiansen, L., Edwards, K., Macdonald, R., Villinger, H., Mottl, M.J., Wheat, C.G., Becker, K., 2003a. Hydrothermal recharge and discharge across 50 km guided by seamounts on a young ridge flank. Nature 421, 618–621. https://doi.org/10.1038/nature01352

Fisher, A.T., Stein, C.A., Harris, R.N., Wang, K., Silver, E.A., Pfender, M., Hutnak, M., Cherkaoui, A., Bodzin, R., Villinger, H., 2003b. Abrupt thermal transition reveals hydrothermal boundary and role of seamounts within the Cocos Plate. Geophysical Research Letters 30. https://doi.org/10.1029/2002GL016766

Froelich, P.N., Klinkhammer, G.P., Bender, M.L., Luedtke, N.A., Heath, G.R., Cullen, D., Dauphin, P., Hammond, D., Hartman, B., Maynard, V., 1979. Early oxidation of organic matter in pelagic sediments of the eastern equatorial Atlantic: suboxic diagenesis. Geochimica et Cosmochimica Acta. 43, 1075–1090. https://doi.org/10.1016/0016-7037(79)90095-4

Gee, J.S., Kent, D. V., 2007. Source of Oceanic Magnetic Anomalies and the Geomagnetic Polarity Timescale, in: Treatise on Geophysics. pp. 455–507. https://doi.org/10.1016/B978-044452748-6.00097-3

Gieskes, J.M., Elderfiled, H., Lawrence, J.R., Johnson, J., Meyers, B., Campbell, A., 1982. Geochemistry of Interstitial Waters and Sediments, Leg 64, Gulf of California, in: Initial Reports of the Deep Sea Drilling Project, 64. https://doi.org/10.2973/dsdp.proc.64.116.1982

Gieskes, J.M., Schrag, D., Chan, L.-H., Zhang, L., Murray, R.W., 1998. Geochemistry of interstitial waters, in: Proceedings of the Ocean Drilling Program, 152 Scientific Results. https://doi.org/10.2973/odp.proc.sr.152.228.1998

Gingele, F.X., Zabel, M., Kasten, S., Bonn, W.J., Nürnberg, C.C., 1999. Biogenic Barium as a Proxy for Paleoproductivity: Methods and Limitations of Application, in: Use of Proxies in Paleoceanography. https://doi.org/10.1007/978-3-642-58646-0_13

Gustafson, C., Key, K., Evans, R.L., 2019. Aquifer systems extending far offshore on the U.S. Atlantic margin. Scientific Reports 9, 8709. https://doi.org/10.1038/s41598-019-44611-7

Gulick, S.P.S., Jaeger, J.M., Mix, A.C., Asahi, H., Bahlburg, H., Belanger, C.L., Berbel, G.B.B., Childress, L., Cowan, E., Drab, L., Forwick, M., Fukumura, A., Ge, S., Gupta, S., Kioka, A., Konno, S., LeVay, L.J., März, C., Matsuzaki, K.M., McClymont, E.L., Moy, C., Müller, J., Nakamura, A., Ojima, T., Ribeiro, F.R., Ridgway, K.D., Romero, O.E., Slagle, A.L., Stoner, J.S., St-Onge, G., Suto, I., Walczak, M.D., Worthington, L.L., Bailey, I., Enkelmann, E., Reece, R., Swartz, J.M., 2015. Mid-Pleistocene climate transition drives net mass loss from rapidly uplifting St. Elias Mountains, Alaska. Proceedings of the National Academy of Sciences. 112, 15042–15047. https://doi.org/10.1073/pnas.1512549112

Harrison, B.K., Zhang, H., Berelson, W., Orphan, V.J., 2009. Variations in archaeal and bacterial diversity associated with the sulfate-methane transition zone in continental margin sediments (Santa Barbara Basin, California). Applied and Environmental Microbiology. 75, 1487–1499. https://doi.org/10.1128/AEM.01812-08

Hartmann, M., Nielsen, H., 1968. δ34S-Werte in rezenten Meeressedimenten und ihre Deutung am Beispiel einiger Sedimentprofile aus der westlichen Ostsee. Geologische Rundschau 58, 621–655. https://doi.org/10.1007/BF01820726

Hathaway, J.C., Degens, E.T., 1969. Methane-Derived Marine Carbonates of Pleistocene Age. Science 165, 690–692. https://doi.org/10.1126/science.165.3894.690

Hein, J.R., O'Neil, J.R., Jones, M.G., 1979. Origin of authigenic carbonates in sediment from the deep Bering Sea. Sedimentology 26, 681–705. https://doi.org/10.1111/j.1365-3091.1979.tb00937.x

Hsü, K.J., Ryan, W.B.F., Cita, M.B., 1973. Late miocene desiccation of the mediterranean. Nature 242, 240–244. https://doi.org/10.1038/242240a0

Hsü, K.J., Montadert, L., Bernoulli, D., Cita, M.B., Erickson, A., Garrison, R.E., Kidd,

R.B., Mèlierés, F., Müller, C., Wright, R., 1977. History of the mediterranean salinity crisis. Nature 267, 399–403. https://doi.org/10.1038/267399a0

Hutnak, M., Fisher, A.T., Zühlsdorf, L., Spiess, V., Stauffer, P.H., Gable, C.W., 2006. Hydrothermal recharge and discharge guided by basement outcrops on 0.7-3.6 Ma seafloor east of the Juan de Fuca Ridge: Observations and numerical models. Geochemistry, Geophysics, Geosystems 7. https://doi.org/10.1029/2006GC001242

Jaeger J.M., Gulick S.P.S., LeVay L.J., Asahi H., Bahlburg H., Belanger C.L., Berbel G.B.B., Childress L.B., Cowan E.A., Drab L., Forwick M., Fukumura A., Ge S., Gupta S., Kioka A., Konno S., März C., Matsuzaki K.M., McClymont E.L., Mix A.C., Moy C., Müller J., Nakamura A., Ojima T., Ridgway K.D., Ribeiro F.R., Romero O.E., Slagle A.L., Stoner J.S., St-Onge G., Suto I., Walczak M.D. and Worthington L.L., 2014. Proceedings of the Integrated Ocean Drilling Program Vol. 341: Expedition reports Southern Alaska margin. Integrated Ocean Drilling Program.

Jorgensen, B.B., 1979. A theoretical model of the stable sulfur isotope distribution in marine sediments. Geochimica et Cosmochimica Acta 43, 363-374. https://doi.org/10.1016/0016-7037(79)90201-1

Jorgensen, B.B., 2006. Bacteria and marine biogeochemistry, in: Marine Geochemistry. pp. 169–206. https://doi.org/10.1007/3-540-32144-6_5

Kasten, S., Freudenthal, T., Gingele, F.X., Schulz, H.D., 1998. Simultaneous formation of iron-rich layers at different redox boundaries in sediments of the Amazon deep-sea fan. Geochimica et Cosmochimica Acta 62, 2253–2264. https://doi.org/10.1016/S0016-7037(98)00093-3

Kasten, S., Haese, R.R., Zabel, M., Rühlemann, C., Schulz, H.D., 2001. Barium peaks at glacial terminations in sediments of the equatorial Atlantic Ocean - Relicts of deglacial productivity pulses? Chemical Geology 175, 635–651. https://doi.org/10.1016/S0009-2541(00)00377-6

Kasten, S., Zabel, M., Heuer, V., Hensen, C., 2003. Processes and Signals of Nonsteady-State Diagenesis in Deep-Sea Sediments and their Pore Waters, in: The South Atlantic in the Late Quaternary. pp. 431–459. https://doi.org/10.1007/978-3-642-18917-3_20

Kasten, S., Nöthen, K., Hensen, C., Spieß, V., Blumenberg, M., Schneider, R.R., 2012. Gas hydrate decomposition recorded by authigenic barite at pockmark sites of the northern Congo Fan. Geo-Marine Letters https://doi.org/10.1007/s00367-012-0288-9

Kuhn, T., Versteegh, G.J.M., Villinger, H., Dohrmann, I., Heller, C., Koschinsky, A., Kaul, N., Ritter, S., Wegorzewski, A. V., Kasten, S., 2017. Widespread seawater circulation in 18-22 Ma oceanic crust: Impact on heat flow and sediment geochemistry. Geology 45, 799–802. https://doi.org/10.1130/G39091.1

Kulm L.D. and Von Huene R., 1973. Initial reports of the deep sea drilling project. XVIII: Washington, DC, US Govt. Printing Office.https://doi.org/10.2973/dsdp.proc.18.1973

Larsen, H.C., Saunders, A.D., Clift, P.D., 1994. Introduction: breakup of the

Southeast Greenland Margin and the formation of the Irminger Basin: background and scientific objectives, in: Proceedings of the Ocean Drilling Program, 152 Initial Reports. https://doi.org/10.2973/odp.proc.ir.152.101.1994

Leavitt W.D., 2014. On the mechanisms of sulfur isotope fractionation during microbial sulfate reduction. Earth and Planetary Sciences. Cambridge, MA: Harvard University, ProQuest.http://nrs.harvard.edu/urn-3:HUL.InstRepos:12274566

Leithold, E.L., Blair, N.E., 2001. Watershed control on the carbon loading of marine sedimentary particles. Geochimica et Cosmochimica Acta 65, 2231–2240. https://doi.org/10.1016/S0016-7037(01)00593-2

Li Y.-H. (2000) A compendium of geochemistry: from solar nebula to the human brain. Princeton University Press.

Martens, C.S., Berner, R.A., 1977. Interstitial water chemistry of anoxic Long Island Sound sediments. 1. Dissolved gases. Limnology and Oceanography 22, 10-25. https://doi.org/10.4319/lo.1977.22.1.0010

Martin, J.H., 1990. Glacial-interglacial CO2 change: The Iron Hypothesis. Paleoceanography 5, 1–13. https://doi.org/10.1029/PA005i001p00001

März, C., Hoffmann, J., Bleil, U., de Lange, G.J., Kasten, S., 2008. Diagenetic changes of magnetic and geochemical signals by anaerobic methane oxidation in sediments of the Zambezi deep-sea fan (SW Indian Ocean). Marine Geology 255, 118–130. https://doi.org/10.1016/j.margeo.2008.05.013

März, C., Poulton, S.W., Brumsack, H.J., Wagner, T., 2012. Climate-controlled variability of iron deposition in the Central Arctic Ocean (southern Mendeleev Ridge) over the last 130,000 years. Chemical Geology 330–331, 116–126. https://doi.org/10.1016/j.chemgeo.2012.08.015

März, C., Riedinger, N., Sena, C., Kasten, S., 2018. Phosphorus dynamics around the sulphate-methane transition in continental margin sediments: Authigenic apatite and Fe(II) phosphates. Marine Geology 404, 84-96. https://doi.org/10.1016/j.margeo.2018.07.010

Masson, D.G., 1991. Fault patterns at outer trench walls. Marine Geophysical Researches 13, 209–225. https://doi.org/10.1007/BF00369150

Meister, P., Liu, B., Ferdelman, T.G., Jørgensen, B.B., Khalili, A., 2013. Control of sulphate and methane distributions in marine sediments by organic matter reactivity. Geochimica et Cosmochimica Acta 104, 183–193. https://doi.org/10.1016/j.gca.2012.11.011

Meyers, P.A., Shaw, T.J., 1996. Organic matter accumulation, sulfate reduction, and methanogenesis in Pliocene–Pleistocene turbidites on the Iberian Abyssal Plain, in: Proceedings of the Ocean Drilling Program, 149 Scientific Results. https://doi.org/10.2973/odp.proc.sr.149.258.1996

Meyers, P.A., Silliman, J.E., Shaw, T.J., 1996. Effects of turbidity flows on organic matter accumulation, sulfate reduction, and methane generation in deep-sea sediments on the Iberia Abyssal Plain, Organic Geochemistry 25, 69-78. https://doi.org/10.1016/S0146-6380(96)00106-4

Middelburg, J.J., de Lange, G.J., Kreulen, R., 1990. Dolomite formation in anoxic sediments of Kau Bay, Indonesia. Geology 18, 399-402. https://doi.org/10.1130/0091-7613(1990)018<0399:DFIASO>2.3.CO;2

Naif, S., Key, K., Constable, S., Evans, R.L., 2015. Water-rich bending faults at the Middle America Trench. Geochemistry, Geophysics, Geosystems 16, 2582–2597. https://doi.org/10.1002/2015GC005927

Niewöhner, C., Hensen, C., Kasten, S., Zabel, M., Schulz, H.D., 1998. Deep sulfate reduction completely mediated by anaerobic methane oxidation in sediments of the upwelling area off Namibia. Geochimica et Cosmochimica Acta 62, 455–464. https://doi.org/10.1016/S0016-7037(98)00055-6

Ono, S., 2008. Multiple-sulphur isotope biosignatures. Space Science Reviews 135, 203–220. https://doi.org/10.1007/s11214-007-9267-2

Parkes, R.J., Webster, G., Cragg, B.A., Weightman, A.J., Newberry, C.J., Ferdelman, T.G., Kallmeyer, J., Jørgensen, B.B., Aiello, I.W., Fry, J.C., 2005. Deep sub-seafloor prokaryotes stimulated at interfaces over geological time. Nature 436, 390–394. https://doi.org/10.1038/nature03796

Peketi, A., Mazumdar, A., Joshi, R.K., Patil, D.J., Srinivas, P.L., Dayal, A.M., 2012. Tracing the Paleo sulfate-methane transition zones and H<inf>2</inf>S seepage events in marine sediments: An application of C-S-Mo systematics. Geochemistry, Geophysics, Geosystems 13. https://doi.org/10.1029/2012GC004288

Pfeifer, K., Kasten, S., Hensen, C., Schulz, H.D., 2001. Reconstruction of primary productivity from the barium contents in surface sediments of the South Atlantic Ocean, in: Marine Geology. https://doi.org/10.1016/S0025-3227(01)00121-9

Pierre, C., Blanc-Valleron, M.M., Caquineau, S., März, C., Ravelo, A.C., Takahashi, K., Alvarez Zarikian, C., 2016. Mineralogical, geochemical and isotopic characterization of authigenic carbonates from the methane-bearing sediments of the Bering Sea continental margin (IODP Expedition 323, Sites U1343-U1345). Deep-Sea Research Part II: Topical Studies in Oceanography 125–126, 133–144. https://doi.org/10.1016/j.dsr2.2014.03.011

Poulton, S.W., Canfield, D.E., 2005. Development of a sequential extraction procedure for iron: Implications for iron partitioning in continentally derived particulates. Chemical Geology 214, 209–221. https://doi.org/10.1016/j.chemgeo.2004.09.003

Poulton, S.W., Krom, M.D., Raiswell, R., 2004. A revised scheme for the reactivity of iron (oxyhydr)oxide minerals towards dissolved sulfide. Geochimica et Cosmochimica Acta 68, 3703–3715. https://doi.org/10.1016/j.gca.2004.03.012

Raiswell, R., Canfield, D.E., 1998. Sources of iron for pyrite formation in marine sediments. American Journal of Science 298, 219–245. https://doi.org/10.2475/ajs.298.3.219

Reeburgh, W.S., 1980. Anaerobic methane oxidation: Rate depth distributions in Skan Bay sediments. Earth and Planetary Science Letters 47, 345–352. https://doi.org/10.1016/0012-821X(80)90021-7

Reece, R.S., Gulick, S.P.S., Horton, B.K., Christeson, G.L., Worthington, L.L., 2011. Tectonic and climatic influence on the evolution of the Surveyor Fan and Channel system, Gulf of Alaska. Geosphere 7, 830–844. https://doi.org/10.1130/GES00654.1

Reece, R.S., Gulick, S.P.S., Christeson, G.L., Horton, B.K., Van Avendonk, H., Barth, G., 2013. The role of farfield tectonic stress in oceanic intraplate deformation, Gulf of Alaska. Journal of Geophysical Research: Solid Earth 118, 1862–1872. https://doi.org/10.1002/jgrb.50177

Riedinger, N., Pfeifer, K., Kasten, S., Garming, J.F.L., Vogt, C., Hensen, C., 2005. Diagenetic alteration of magnetic signals by anaerobic oxidation of methane related to a change in sedimentation rate. Geochimica et Cosmochimica Acta 69, 4117–4126. https://doi.org/10.1016/j.gca.2005.02.004

Riedinger, N., Kasten, S., Gröger, J., Franke, C., Pfeifer, K., 2006. Active and buried authigenic barite fronts in sediments from the Eastern Cape Basin. Earth and Planetary Science Letters 241, 876–887. https://doi.org/10.1016/j.epsl.2005.10.032

Rudnicki, M.D., Elderfield, H., Spiro, B., 2001. Fractionation of sulfur isotopes during bacterial sulfate reduction in deep ocean sediments at elevated temperatures. Geochimica et Cosmochimica Acta 65, 777–789. https://doi.org/10.1016/S0016-7037(00)00579-2

Schlitzer, R., 2015. Ocean Data View. http://odv.awi.de

Shillington, D.J., 2018. Water takes a deep dive into an oceanic tectonic plate. Nature 563, 335-336. https://doi.org/10.1038/d41586-018-07335-8

Sim, M.S., Bosak, T., Ono, S., 2011. Large sulfur isotope fractionation does not require disproportionation. Science 333, 74–77. https://doi.org/10.1126/science.1205103

Strauss, H., 1997. The isotopic composition of sedimentary sulfur through time. Palaeogeography, Palaeoclimatology, Palaeoecology 132 97-118. https://doi.org/10.1016/S0031-0182(97)00067-9

Strauss, H., 1999. Geological evolution from isotope proxy signals - Sulfur. Chemical Geology 161, 89–101. https://doi.org/10.1016/S0009-2541(99)00082-0

Strauss, H., Bast, R., Cording, A., Diekrup, D., Fugmann, A., Garbe-Schönberg, D., Lutter, A., Oeser, M., Rabe, K., Reinke, D., Teichert, B.M.A., Westernströer, U., 2012. Sulphur diagenesis in the sediments of the Kiel Bight, SW Baltic Sea, as reflected by multiple stable sulphur isotopes. Isotopes in Environmental and Health Studies 48, 166–179. https://doi.org/10.1080/10256016.2012.648930

Torres, M.E., Bohrmann, G., Suess, E., 1996. Authigenic barites and fluxes of barium associated with fluid seeps in the Peru subduction zone. Earth and Planetary Science Letters 144, 469–481. https://doi.org/10.1016/S0012-821X(96)00163-X

Torres, M.E., Cox, T., Hong, W.L., Mcmanus, J., Sample, J.C., Destrigneville, C., Gan, H.M., Gan, H.Y., Moreau, J.W., 2015. Crustal fluid and ash alteration impacts on the biosphere of Shikoku Basin sediments, Nankai Trough, Japan.

Geobiology 13, 562–580. https://doi.org/10.1111/gbi.12146

Treude, T., Krause, S., Maltby, J., Dale, A.W., Coffin, R., Hamdan, L.J., 2014. Sulfate reduction and methane oxidation activity below the sulfate-methane transition zone in Alaskan Beaufort Sea continental margin sediments: Implications for deep sulfur cycling. Geochimica et Cosmochimica Acta 144, 217–237. https://doi.org/10.1016/j.gca.2014.08.018

Turner, D.L., Forbes, R.B., Naeser, C.W., 1973. Radiometric ages of kodiak seamount and giacomini guyot, gulf of alaska: implications for circum-pacific tectonics. Science 182, 579–81. https://doi.org/10.1126/science.182.4112.579

Vandenbroucke, M., Largeau, C., 2007. Kerogen origin, evolution and structure. Organic Geochemistry 38, 719-833. https://doi.org/10.1016/j.orggeochem.2007.01.001

Von Breymann, M.T., Emeis, K.-C., Suess, E., 1992. Water depth and diagenetic constraints on the use of barium as a palaeoproductivity indicator. Geological Society, London, Special Publications, 64, 273–284. https://doi.org/10.1144/GSL.SP.1992.064.01.18

Waterman, L. S., Sayles, F. L., Manheim, F. T., 1973. Interstitial water studies on small core samples, Legs 16, 17, and 18. Initial Reports of the Deep Sea Drilling Project. Vol. 18. US Gov. Print. Off Washington, DC, 1973. 1001-1012. https://doi.org/10.2973/dsdp.proc.18.app2.1973

Wedepohl, K.H., 1971. Environmental influences on the chemical composition of shales and clays. Physics and Chemistry of the Earth https://doi.org/10.1016/0079-1946(71)90020-6

Wedepohl, K.H., 1991. Chemical composition and fractionation of the continental crust. Geologische Rundschau 80, 207–223. https://doi.org/10.1007/BF01829361

Wehrmann, L.M., Ockert, C., Mix, A.C., Gussone, N., Teichert, B.M.A., Meister, P., 2016. Repeated occurrences of methanogenic zones, diagenetic dolomite formation and linked silicate alteration in southern Bering Sea sediments (Bowers Ridge, IODP Exp. 323 Site U1341). Deep-Sea Research Part II: Topical Studies in Oceanography 125–126, 117–132. https://doi.org/10.1016/j.dsr2.2013.09.008

Wortmann, U.G., Bernasconi, S.M., Böttcher, M.E., 2001. Hypersulfidic deep biosphere indicates extreme sulfur isotope fractionation during single-step microbial sulfate reduction. Geology 29, 647–650. https://doi.org/10.1130/0091-7613(2001)029<0647:HDBIES>2.0.CO;2

Figure Captions:

Figure 1: Bathymetric map showing position of Sites U1417 and U1418 IODP Expedition 341 and Site 178 DSDP Leg 18; red line across Site U1417 indicates seismic profile of Figure 2; arrow indicates direction of Pacific Plate movement (DeMets et al., 2010). Map created with Ocean Data view (Schlitzer, 2015).

Figure 2: Seismic profile shown in seconds two-way travel time across Site U1417; position indicated by red line A - A' in Figure 1. Blue dashed line indicates borehole position, green line represents gamma ray downhole logging (Jaeger et al., 2014). Note presence of plate bending-related normal faults offsetting sediments from the seafloor to the top of ocean crust within the sediment adjacent to Site U1417 indicated by arrows. Basement occurs in ~6310 s TWT.

Figure 3: From (Jaeger et al., 2014): pore-water downcore profiles of SO_4^{2-}, pore-gas CH_4, pore-water total alkalinity, NH_4 (all in mM), Ba^{2+}, Fe^{2+}, Li^{+}, Sr^{2+} (all in µM) Ca^{2+} and Mg^{2+}(in mM). Dashed lines indicate seawater concentrations (Li, 2000).

Figure 4: Geochemical data at Site U1417. Sedimentary downcore profiles of TOC, Si, Al, Fe, S (all as wt%), Ba, Zr (both in mg/kg sediment), TOC (wt%), Si/Al, Zr/Al and sedimentation rate (in m/Ma). Dashed vertical lines indicate average shale contents (Wedepohl, 1971, 1991).

Figure 5: Fe and S speciation data. Fe/Al, S/Al, Fe-S/FeT, Fe HR/FeT and Fe-S/Fe HR ratios (all as g/g).

Figure 6: Geochemical data relevant for authigenic mineral formation. Pore-water SO_4^{2-}*, pore-gas* CH_4 *(all* in *mM), Ba/Al, Pore-water* Ba^{2+} *(in µM),* $CaCO_3$ *(in wt%),* $\delta^{34}S_{py}$ *(‰), vertical dashed line indicates zero-reference V-CDT standard. Gray shadings indicate three distinguished diagenetic zones.*

Figure 7: Pseudo-Van-Krevelen Plot for Site U1417 below 600 m CCSF-B. Numbers indicate depth of individual sample in mbsf CCSF-B. Data from Childress (2016). Roman numbers indicate kerogen type (Vandebroucke and Largeau, 2007).

Figure 8: Comparison of TOC profiles (in wt %) and pore-water profiles of sulfate, total alkalinity (TA), Ca^{2+}*,* Mg^{2+} *(in mM),* Ba^{2+} *and* Sr^{2+} *(in µM) from DSDP Site 178 (red dots) and IODP Site U1417 (black dots). IODP TOC data from this study, IODP pore-water data from Jaeger et al. (2014), DSDP data from Kulm and Von Huene (1973).*

Figure 9: Schematic illustration of mechanism to create deep aquifer by plate bending faults (not to scale).

Highlights:

1) Site U1417 in the Gulf of Alaska shows uncommon diagenetic profile
2) No shallow sulfate-methane transition zone formed
3) Methane consumption by barite dissolution prevents upward methane diffusion
4) Deep, reversed sulfate-methane transition fuelled by deep aquifer
5) Deep aquifer potentially fed through plate bending faults

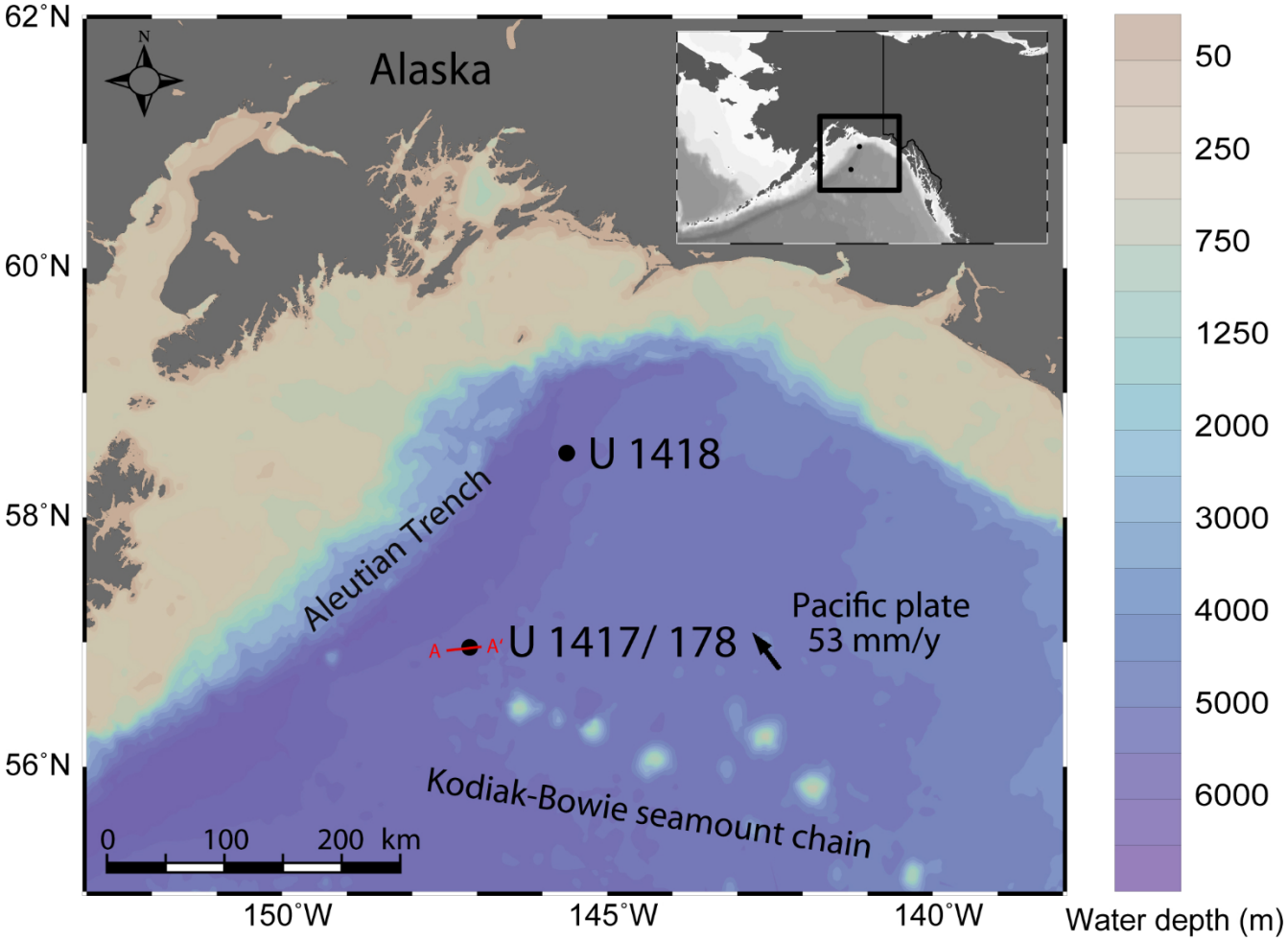
62˚N
60˚N
58˚N
56˚N
150˚W
145˚W
140˚W
N
Alaska
U 1418
Aleutian Trench
A
A'
U 1417/ 178
Pacific plate
53 mm/y
Kodiak-Bowie seamount chain
0
100
200 km
50
250
750
1250
2000
3000
4000
5000
6000
Water depth (m)

Figure 1

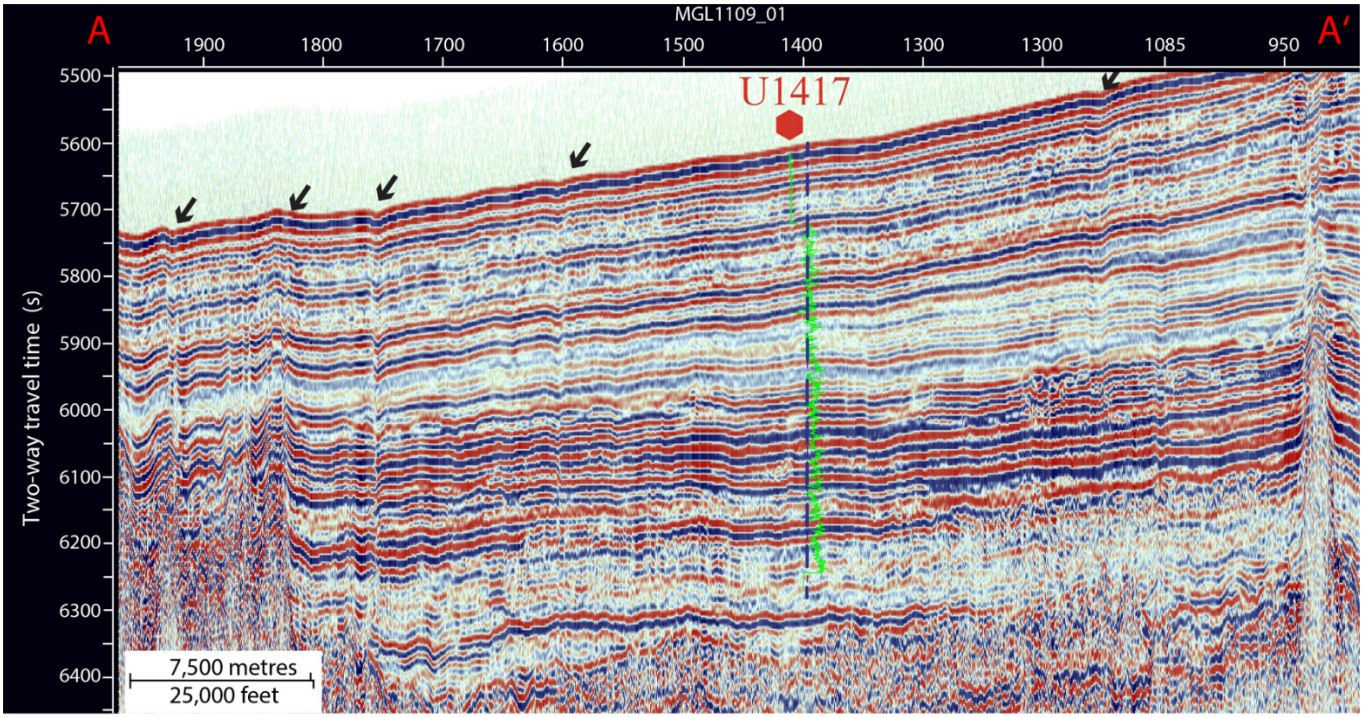
A
MGL1109_01
A′
1900
1800
1700
1600
1500
1400
1300
1300
1085
950
U1417
Two-way travel time (s)
5500
5600
5700
5800
5900
6000
6100
6200
6300
6400
7,500 metres
25,000 feet

Figure 2

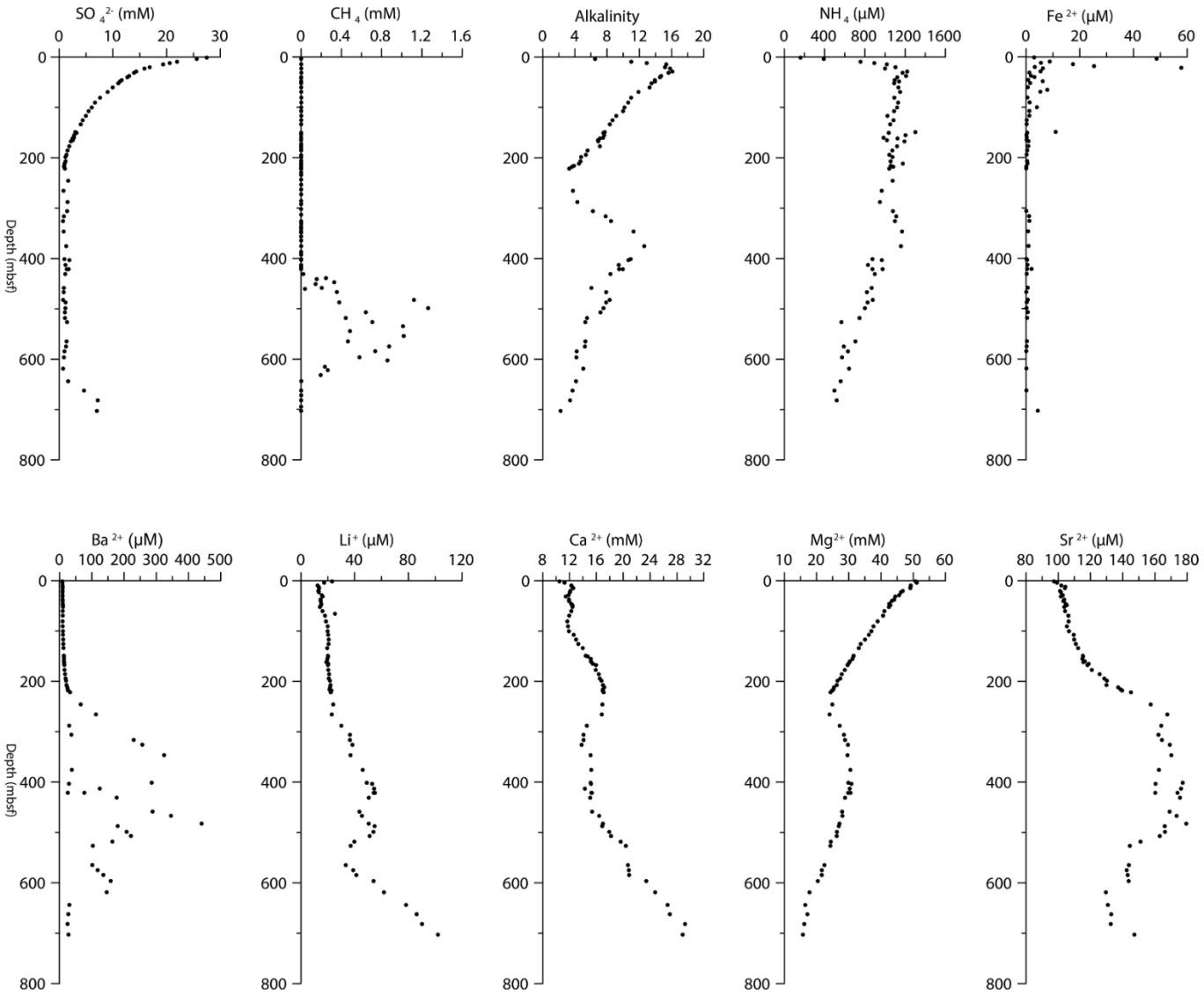
SO 4 2- (mM)
0 10 20 30
CH 4 (mM)
0 0.4 0.8 1.2 1.6
Alkalinity
0 4 8 12 16 20
NH 4 (μM)
0 400 800 1200 1600
Fe 2+ (μM)
0 20 40 60
Depth (mbsf)
0 200 400 600 800
Ba 2+ (μM)
0 100 200 300 400 500
Li+ (μM)
0 40 80 120
Ca 2+ (mM)
8 12 16 20 24 28 32
Mg2+ (mM)
10 20 30 40 50 60
Sr 2+ (μM)
80 100 120 140 160 180

Figure 3

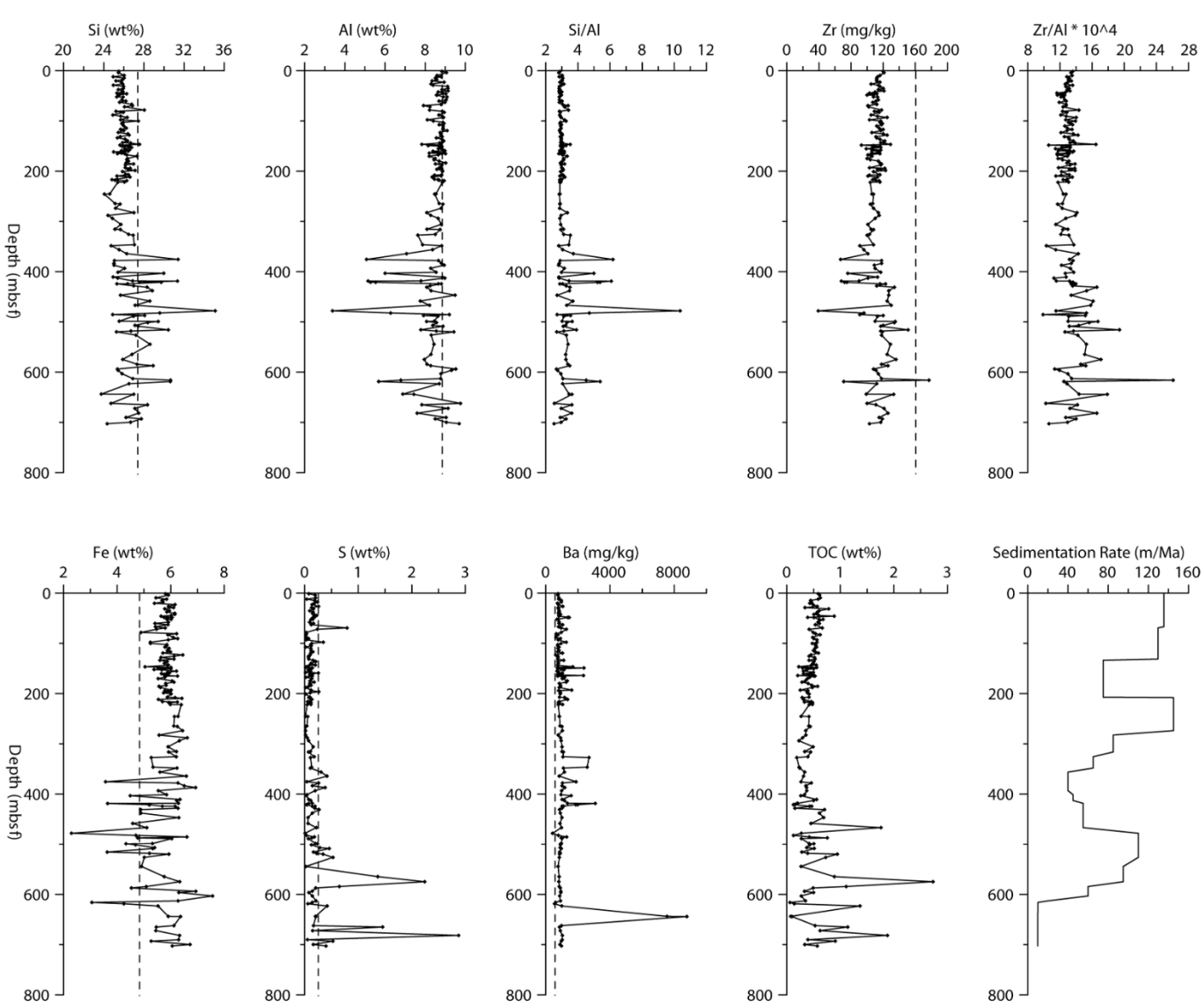
Si (wt%)
20 24 28 32 36
Al (wt%)
2 4 6 8 10
Si/Al
2 4 6 8 10 12
Zr (mg/kg)
0 40 80 120 160 200
Zr/Al * 10^4
8 12 16 20 24 28
Depth (mbsf)
0 200 400 600 800
Fe (wt%)
2 4 6 8
S (wt%)
0 1 2 3
Ba (mg/kg)
0 4000 8000
TOC (wt%)
0 1 2 3
Sedimentation Rate (m/Ma)
0 40 80 120 160

Figure 4

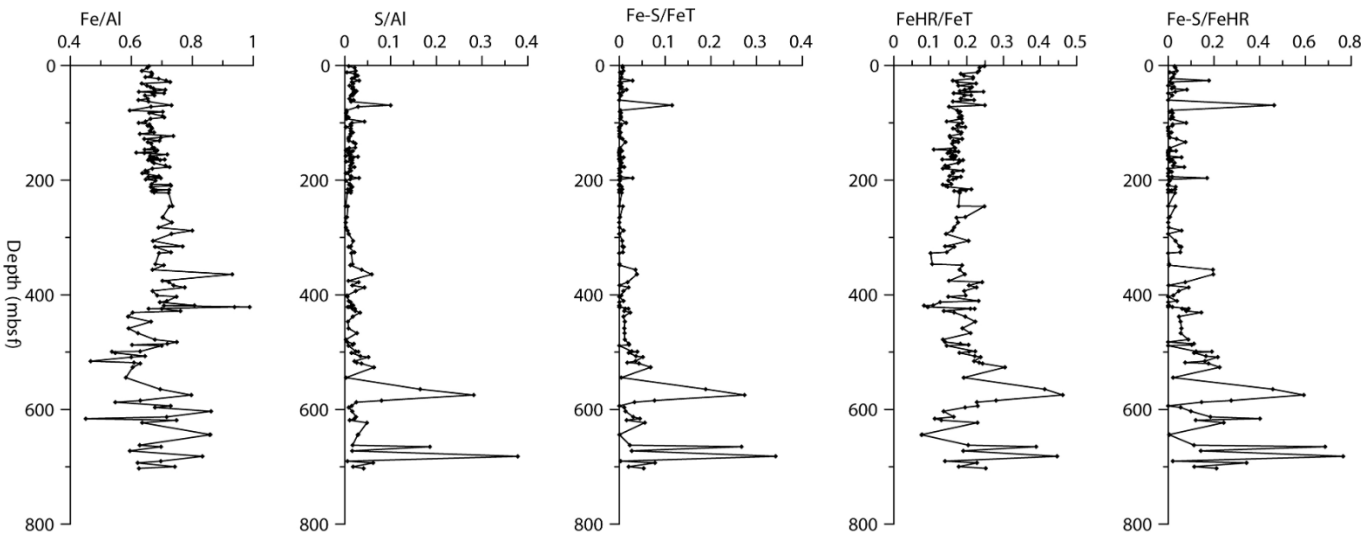
Fe/Al
0.4
0.6
0.8
1
S/Al
0
0.1
0.2
0.3
0.4
Fe-S/FeT
0
0.1
0.2
0.3
0.4
FeHR/FeT
0
0.1
0.2
0.3
0.4
0.5
Fe-S/FeHR
0
0.2
0.4
0.6
0.8
Depth (mbsf)
0
200
400
600
800

Figure 5

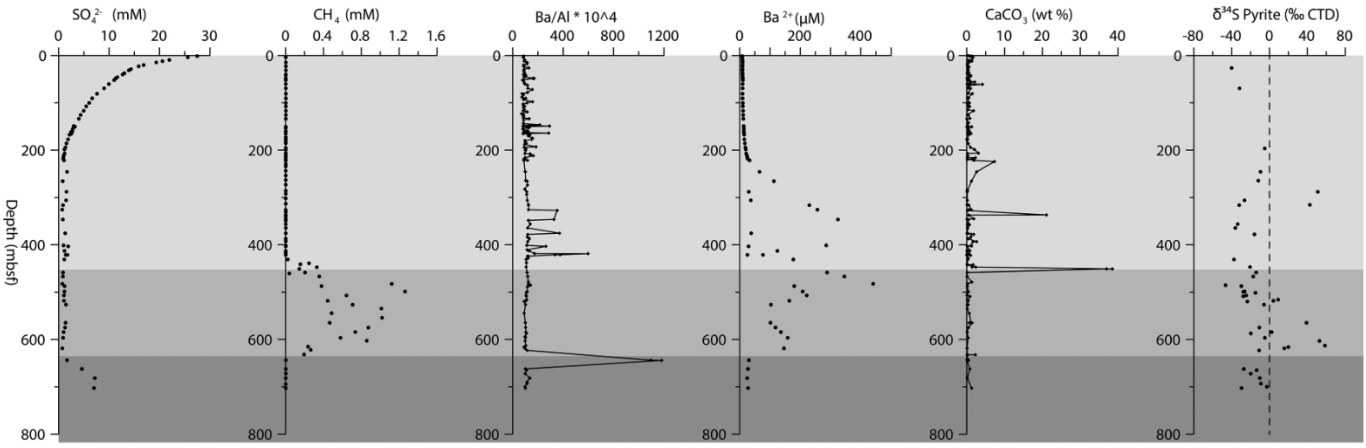
SO_4^{2-} (mM)
0 10 20 30
CH_4 (mM)
0 0.4 0.8 1.2 1.6
Ba/Al * 10^4
0 400 800 1200
Ba^{2+} (µM)
0 200 400
$CaCO_3$ (wt %)
0 10 20 30 40
$\delta^{34}S$ Pyrite (‰ CTD)
-80 -40 0 40 80
Depth (mbsf)
0 200 400 600 800

Figure 6

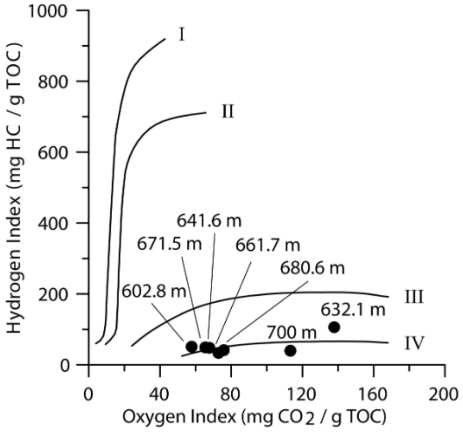
1000
800
600
400
200
0
Hydrogen Index (mg HC / g TOC)
I
II
III
IV
641.6 m
671.5 m
661.7 m
680.6 m
602.8 m
632.1 m
700 m
0
40
80
120
160
200
Oxygen Index (mg CO2 / g TOC)

Figure 7

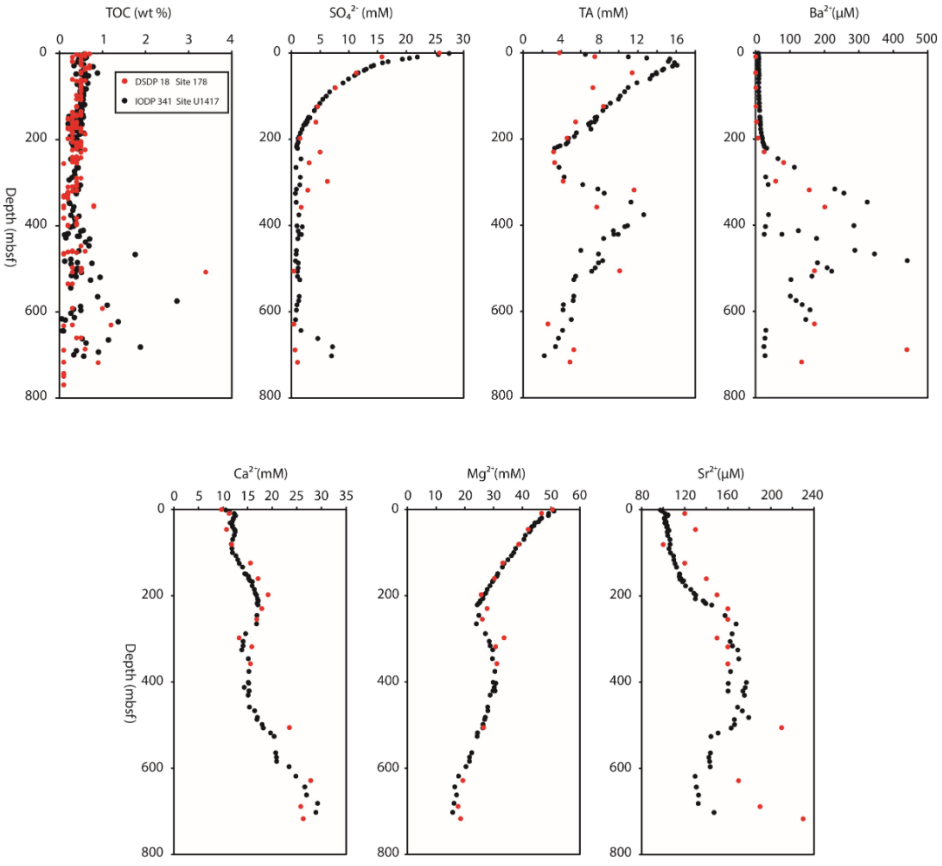
TOC (wt %)
SO_4^{2-} (mM)
TA (mM)
Ba^{2+}(μM)
DSDP 18 Site 178
IODP 341 Site U1417
Depth (mbsf)
Ca^{2+}(mM)
Mg^{2+}(mM)
Sr^{2+}(μM)
Depth (mbsf)

Figure 8

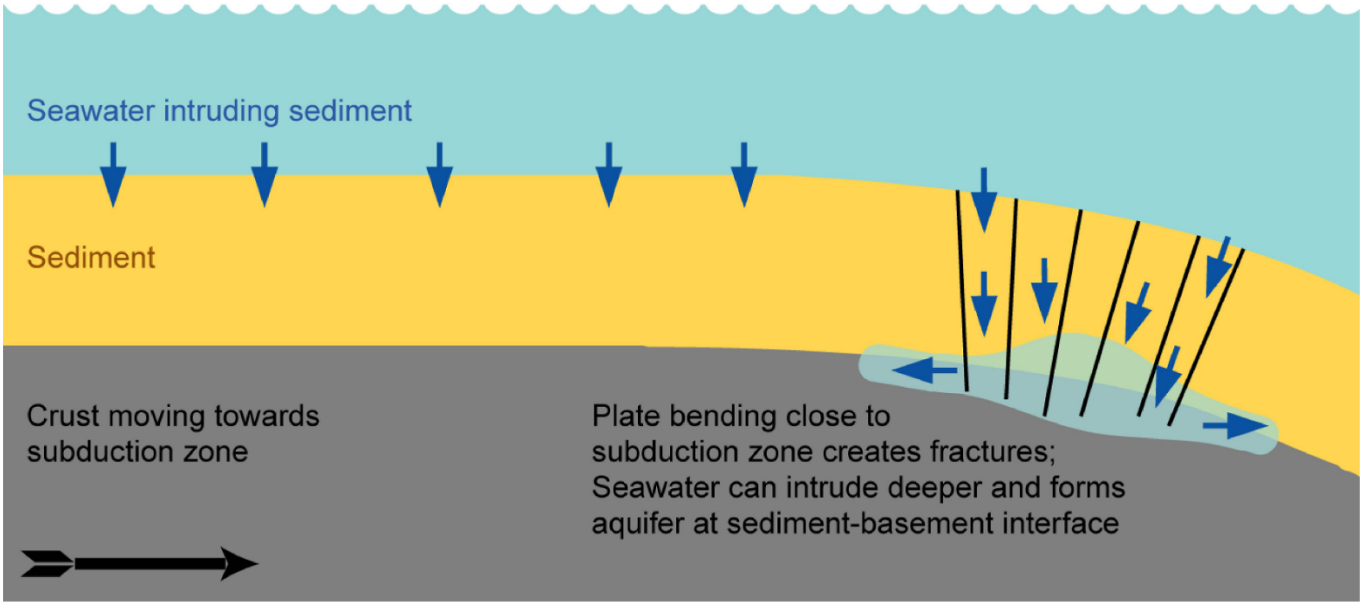
Seawater intruding sediment
Sediment
Crust moving towards subduction zone
Plate bending close to subduction zone creates fractures; Seawater can intrude deeper and forms aquifer at sediment-basement interface

Figure 9